Chapter 5
A Review of Wind-Noise Reduction Methodologies

Kristoffer T. Walker and Michael A.H. Hedlin

5.1 Introduction

5.1.1 Importance of Infrasound in Science and Monitoring

Infrasound and longer-period acoustic gravity waves have been of considerable interest since barometers around the world inadvertently recorded infrasound from the 1883 eruption of Krakatau (Evers and Haak 2010). Early recordings showed that, at low frequencies, there is relatively little intrinsic attenuation, facilitating the detection and characterization of large events over great ranges (e.g., Landau and Lifshitz 1959). Infrasound was used to locate enemy artillery in WWI. Infrasound was used as a monitoring tool during the early proliferation of nuclear weapon technologies after WWII when nuclear tests were routinely conducted in the atmosphere. In 1963, the Limited Test Ban Treaty was signed by most nations, and nuclear testing generally went underground. Interest in infrasound as a monitoring tool waned as interest in global seismology increased.

In 1996, the Comprehensive Nuclear-Test-Ban Treaty (CTBT) opened for signature. This treaty is intended to prohibit all nuclear weapon test explosions. Many countries have signed the treaty, but not ratified it. Ratification is an essential step before the treaty can enter into force. The International Monitoring System (IMS) began construction shortly after the treaty was opened for signature. This system will ultimately comprise more than 300 seismic, hydroacoustic, radionuclide, and infrasound stations. Specifically, each of the 60 infrasound stations will comprise an array of infrasound sensors to determine the direction from which signals originated (Christie 1999).

Since the signing of the CTBT and development of the global IMS infrasound network, there has been a renewed interest in infrasound for monitoring and

K.T. Walker (✉)
Institute of Geophysics and Planetary Physics, University of California, San Diego, 9500 Gilman Drive, La Jolla, CA, 92093, USA
e-mail: walker@ucsd.edu

A. Le Pichon et al. (eds.), *Infrasound Monitoring for Atmospheric Studies*,
DOI 10.1007/978-1-4020-9508-5, © Springer Science+Business Media B.V. 2010

scientific research (Christie and Campus 2010; Campus and Christie 2010). In most of these studies, a very limiting constraint is wind; as wind speed increases, the ability to detect infrasound is compromised. For monitoring purposes, this means that each infrasound array in the IMS network has a detection threshold that varies significantly, if not greatly, with local wind speed. Therefore, at any point in time, a certain percentage of the otherwise fully operational network may not be "mission capable." Carefully evaluated and independently verified techniques to reduce the impact of wind on infrasound detection and characterization are of critical importance to the basic infrasound monitoring and research efforts.

5.1.2 Observations of Wind Noise During Measurements of Infrasound

It has been well known for a long time that noise increases on microphones and microbarometers with increasing winds. Figure 5.1 shows a simple example of infrasound in the 1–20 Hz range recorded at Piñon Flat Observatory by a Brüel & Kjær (B&K) microphone with a standard sponge wind filter at a height of 50 cm above the ground in the presence of wind. These spectra are a result of averaging the Fourier transforms of two-minute windows where the median wind speed was in one of four bins (0–2, 2–4, 4–6, and 6–8 m/s). The 7 m/s bin had far fewer spectra than the other three bins. The leveling off at 1 Hz is due to the instrument response of the microphone. The noise in this case generally increases uniformly by ~5 dB per m/s. Estimates at frequencies of 0.01–0.5 Hz vary from 2 to 7 dB per m/s (McDonald et al. 1971; McDonald and Herrin

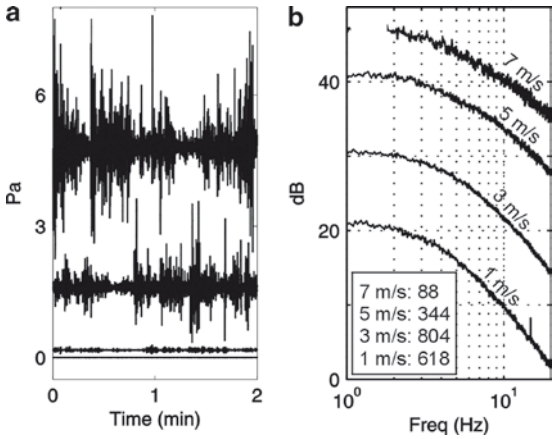

Fig. 5.1 Infrasound recordings in the 1–10 Hz band. Time series (**a**) and average spectra from many 2-min time series (**b**) are shown for four different wind speeds

1974; Hedlin and Alcoverro 2005). Indeed, a 0.05-Pa infrasound signal clearly recorded in 1 m/s winds would be completely masked in 4–5 m/s winds without a better wind filter.

5.2 Wind-Noise Theory

5.2.1 The Physics of Wind

To understand the wind-related noise and design wind-noise resistant technologies or stations, it is helpful to review the basic physics of wind. Wind is caused by spatial differences in atmospheric pressure and is a common part of the diurnal meteorological cycle in most parts of the world. Much of the following discussion comes from Panofsky and Dutton (1984). The first 1–2 km above the ground is called the "friction layer" or the "planetary boundary layer" (PBL), after Lettau (1939). The PBL is defined by the vertical exchange of momentum, heat, and moisture due to surface effects. The top of this layer is often visible to airplane pilots because it contains dust, smoke, and aerosols. The thickness of the PBL can also be detected by acoustic sounders in the 1–3 kHz range and is predicted by a linear relationship with wind speed at 10 m height (e.g., Koracin and Berkowicz 1988).

Wind is intimately related to atmospheric turbulence. There are two types of turbulence: convective and mechanical. Convective turbulence is driven by thermal instability and is the predominant mechanism of mixing in the troposphere. Clouds are often a manifestation of this turbulence. Mechanical turbulence is created by the interaction of the wind with topography and ground-based objects.

A vertical profile in which temperature increases with height is an "inversion" (Fig. 5.2). During the day, solar heating warms the surface and the lower PBL, the top of which occurs at the height z_i. This is the height to the lowest inversion, where the sign of the temperature gradient changes. Because the warmer air near the surface is gravitationally unstable, both convective and mechanical turbu-

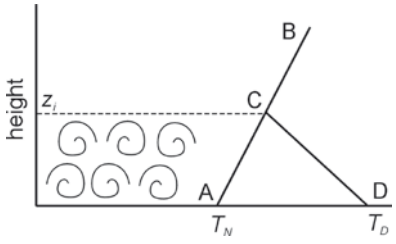

Fig. 5.2 Temperature profiles during the night (AB; inversion) and day (BCD; inversion between CB). The temperature in the surface layer warms during the day, which is one mechanism for driving wind. T_n and T_d are the nighttime and daytime temperatures, respectively

Table 5.1 Surface roughness values (from Panofsky and Dutton 1984)

Ground cover	Roughness length (m)
Water or ice[a]	10^{-4}
Mown grass	10^{-2}
Long grass, rocky ground	0.05
Pasture land	0.20
Suburban housing	0.6
Forests, cities	1–5

[a]Surface roughness increases with wind speed over water

lence occur at a variety of scales producing wind. In some cases, the scales are quite large because of geographical differences in surface heating and can lead to regional horizontal winds. Nonetheless, smaller scale turbulence occurs and defines a mixing layer (surface layer) of thickness h, which is approximately equal to z_i during the day.

An inversion often extends down to the surface at night, making the air gravitationally stable (Fig. 5.2). Consequently, wind and turbulence are often less pronounced at night. However, minor mechanical turbulence still occurs in the lower portions of the surface layer ($h < 100$ m) on clear nights with weak winds.

"Turbules" are defined as self-similar localized eddies (e.g., deWolf 1983; McBride et al. 1992; Goedecke and Auvermann 1997). Wind speed varies as a function of height because of surface friction. In pure mechanical turbulence, the winds in the surface layer are the slowest at the ground level and increase logarithmically with height (e.g., Thuillier and Lappe 1964; Chen 1997). In convective turbulence, the variation of wind speed with height can be much more complex and is often described by a power law over some height range. In either case, the reduction in speed at ground level is a function of the surface roughness, a length that characterizes the size of mechanical turbules (Table 5.1). The surface roughness is also a measure of how efficiently momentum is transferred from the wind into the ground. For example, a dense forest or craggily mountainous terrain has a high roughness and can lead to a great reduction in surface wind. Above relatively smooth surfaces, one can expect a significant increase in wind speed simply between 1 and 3 m height. For example, Berman and Stearns (1977) recorded an ~20–40% difference in wind speed between these two heights in light winds (2–5 m/s).

5.2.2 Predicting Turbulence Potential from Meteorological Data

The potential for turbulence can be calculated from basic meteorological data. Because both mechanical and thermal forcing influences turbulence, a predictive measurement is needed that superimposes the effects of both. Monin and Obukhov

(1954) derived two scaling parameters in the surface layer. The first is the surface friction velocity

$$u_* = \sqrt{\tau / \rho}, \tag{5.1}$$

where ρ is the density and the surface Reynolds stress is $\tau = \rho K_{\mathrm{m}} \partial \overline{u_{\mathrm{x}}} / \partial z$, where $\overline{u_x}$ is the mean wind speed in the wind direction and K_m is the eddy viscosity of the order 1 $\mathrm{m^2\,s^{-1}}$. The second scaling parameter is the Monin-Obukhov length

$$L = -\frac{u_*^3 c_p \rho T}{k_{\mathrm{a}} g H (1 + 0.07 / B)}, \tag{5.2}$$

where c_p is the specific heat at constant pressure, T is the temperature, k_a is the von Karman constant, g is the acceleration due to gravity, H is the vertical heat flux, and B is the Bowen ratio

$$B = -\frac{T_H - T_L + 0.01\Delta z}{2500(q_H - q_L)}, \tag{5.3}$$

where T and q are temperature and humidity at a high and low reference point separated by Δz in the surface layer. In general, L is essentially independent of height, is computed from near-surface measurements, and varies mostly because of variations in u_* and H.

The important parameter that superimposes the effects of thermal and mechanical forcing is the ratio z/L, where z is the height above the ground. This ratio is a measure of the relative importance of mechanical and thermal forcing in the characterization of atmospheric stability. Strongly negative values indicate a dominance of convective turbulence. Smaller negative values are associated with a dominance of mechanical turbulence. Zero means there is pure mechanical turbulence (theoretical case at the ground level). Slightly positive values suggest mechanical turbulence is damped by temperature stratification. Strongly positive values indicate strong damping of turbulence.

5.2.3 *Geographic Influences on Wind*

Careful site selection as a strategy for the abatement of wind noise can benefit greatly from knowledge of the local wind patterns. Much of this section is from Pidwirny and Budikova (2006). As mentioned earlier, wind is derived by spatial differences in atmospheric pressure, which are usually directly related to changes in temperature due to solar heating and surface radiation. Because these differences occur at a variety of scales, they interfere with each other to give rise to the observed local conditions. At a global scale, the equatorial regions experience more solar heating than at the poles. Warming through conduction and convection, the air flows upward and toward the poles, where cooling causes the air to flow

down to the surface and back to the equatorial regions. As viewed from a frame of reference that is fixed in the forward flow, the Coriolis effect deflects the flow toward the right and the left in the northern and southern hemispheres, respectively, leading to three circulation cells in each hemisphere. This system drives most of the global circulation patterns, which are ultimately modulated by regional and local influences.

In the continental interiors, regional variations in solar heating during the day influence convection patterns. Solar heating of the surface warms the air via conduction, the air ascends, horizontal pressure gradients form, and convection pulls in air from other regions that are cooler, such as those beneath cloud cover (Fig. 5.3). The horizontal winds usually do not travel straight lines between the high- and low-pressure regions because of influences by global circulation patterns. This idealized system only works during the day; at night, there is no variation in surface heating or cooling to drive convection and surface winds.

Coastal environments can lead to a similar pattern of convection during the day. Because of the specific heat capacity of water and mixing with deeper layers, the water surface does not heat up as much as the land surface (Fig. 5.4). This can lead to differential surface/air heating, a horizontal pressure gradient, and onshore surface winds.

Unlike continental interiors, coastal environments can also drive convection systems at night. After sunset, the heated land surface continues to radiate heat and eventually becomes cooler than the air temperature, at which point heat is transferred from the air to the ground. Conversely, the water surface stays at a relatively fixed temperature and continues to transfer heat to the air. This reverses the pattern shown in Fig. 5.4, leading to offshore surface winds.

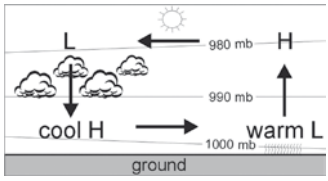

Fig. 5.3 Regional influences on wind in an intracontinental setting during the day. Differences in solar heating at the surface leads to horizontal air temperature and pressure gradients that can lead to a closed convection system

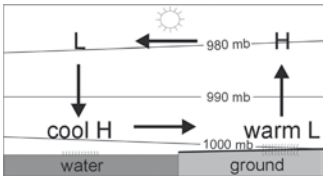

Fig. 5.4 Regional influences on wind in a coastal setting during the day. The specific heat capacity of water leads to differences in solar heating and cooling of the surface, which can drive a close convection system

Whereas the above regional systems are diurnal in nature, there are also seasonal influences on wind over continental spatial scales. In certain equatorial regions, the average daily temperature of the inner continental land surface is greater than that of the adjacent water surfaces. This leads to onshore "Monsoon" winds during the summer that persist diurnally. In some locations and times of the year, these humid winds are diurnally uniform. The situation is reversed during the winter, and the region is dominated by dry offshore winds.

Mountains also affect wind patterns. Despite the obvious obstacle that mountains present to winds driven by global convection systems, mountains also act as sources of heat during the day. Solar heating of their slopes leads to a flow of air up and above the mountain to the height of the surface layer where it is deflected. In the specific case of a valley, heating on both adjacent slopes can give rise to a circulation system with vertical return flow above the axis of the valley. At night, the mountains are heat sinks rather than heat sources; the convection pattern is reversed.

5.2.4 Taylor's Hypothesis

Of fundamental importance to wind-noise theory, Taylor (1938) hypothesized that turbules and their associated observables are spatially fixed time-invariant anomalies. This hypothesis is often called "Taylor's frozen turbulence hypothesis." If correct, this predicts that the statistical properties of flow in time measured at a single point can be used to infer the two-dimensional spatial characteristics of turbulence within the limitations placed by variations of local topography.

There have been numerous verifications of Taylor's hypothesis (e.g., Favre et al. 1962; Frenkiel and Klebanoff 1966; Panofsky 1962). Measurements on aircraft have also been compared to those from towers to test this concept (e.g., Panofsky and Mazzola 1971; Kaimal et al. 1982). These aircraft fly along the mean wind direction so quickly that they effectively sample space instantaneously. The results suggest that short-wavelength structures move with the mean wind (e.g., McDonald et al. 1971), but large-scale structures move at their own velocities in contrast to Taylor's hypothesis.

Although Taylor's hypothesis appears to be generally valid at higher frequencies, studies have shown that turbules are not indefinitely time invariant. Rather, they decay with distance traveled by an amount that is proportional to their length scale; smaller turbules decay faster over shorter distances traveled than larger turbules.

Shields (2005) analyzed pressure data from two strings of microphones located on the ground: one along the wind direction and one perpendicular to it. He calculated the cross-correlation between the reference sensor (the one at the intersection of the two strings) with the other sensors at greater distances in the downwind and crosswind directions (Fig. 5.5). In the downwind direction, what is observed by the reference sensor is observed some time later by the downwind sensors, but the correlation is gradually reduced with time/distance.

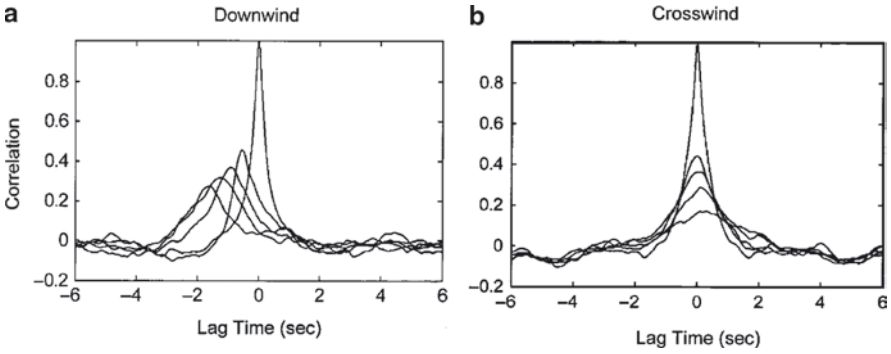

Fig. 5.5 Quantification of Taylor's frozen turbulence hypothesis. Shown are the cross-correlation functions between a reference microphone and microphones at increasing distances in the downwind (**a**) and crosswind (**b**) directions. The sensor separations in the downwind and crosswind directions are 1.2 and 0.6 m, respectively. Modified from Shields (2005)

Indeed, in time/distance space, the slope of the line that connects the points associated with the maxima in (Fig. 5.5a) is equal to the mean advection velocity (~2.7 m/s). If the sensors themselves are not modifying the turbulence, then this suggests Taylor's hypothesis is only a first-order approximation at typical infrasound frequencies. In the crosswind direction, there is also some correlation, but the peak is at zero lag for all sensors, simply reflecting the crosswind spatial coherence length.

5.2.5 Turbulence Length Scales and Noise Spectra

As proposed by Kolmogorov (1941), turbulence velocity spectra are separated into frequency ranges that are associated with three spatial scales of turbulence: source region (large scales and low frequencies), inertial subrange (intermediate scales and frequencies), and dissipation region (small scales and high frequencies). The source region comprises large eddies with length scales of tens of meters to kilometers. The spectral characteristics of this range are not isotropic; the characteristics depend on many variables, including wind, surface roughness, and height of the surface layer. Mixing within the PBL causes energy-containing eddies from the source region to fragment into smaller eddies without energy dissipation. This mixing without dissipation defines the isotropic inertial subrange, with eddy length scales of less than the height above the surface, but larger than the Kolmogorov microscale, which is the smallest scale of turbulence defined by

$$\eta = \left(\frac{\nu^3}{\varepsilon} \right)^{1/4}, \tag{5.4}$$

where ε is the dissipation rate of turbulence into heat and ν is the kinematic (or molecular) viscosity. Continued mixing leads to eddies that are smaller than the Kolmogorov microscale, defining the isotropic dissipation range where molecular mixing dissipates energy over a length scale on the order of millimeter in the surface layer, which is too small to be of concern here.

Wind noise in the infrasound band pertains to the source region and the inertial subrange. Identifying these ranges in spectra of recorded wind noise is important for understanding what type of wind noise is being recorded, which ultimately helps one design or choose the optimum wind-noise filter. For a stationary sensor, the frequency separating the source region on the low side from the inertial subrange on the high side for wind-speed fluctuations in the downwind direction is defined by $fz/\overline{u} > 1$, where f is the frequency, z is the sensor height, and $\bar{u}$ is the mean wind speed (Panofsky and Dutton 1984). Figure 5.6 is a graph depicting this relationship for 10 logarithmically spaced wind speeds. For a fixed wind speed, the inertial subrange moves to lower frequencies as the sensor height increases. For a sensor precisely at the ground level, the inertial subrange is undefined, and the entire infrasound spectrum is in the source region. For a fixed sensor height, the source region moves to higher frequencies as the wind speed increases. The IMS arrays have effective sensor heights from 5 to 40 cm and wind speeds that typically extend up to 5 m/s. Therefore, for any given spectra of recorded pressure, one can expect to find this boundary above ~0.2 Hz. For wind speeds of at least 1 m/s, the boundary is above ~3 Hz.

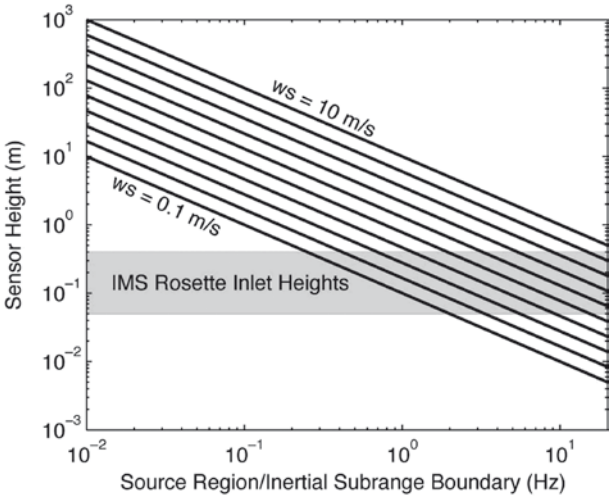

Fig. 5.6 Frequency boundary between the source region at the low end and the inertial subrange at the high end as a function of wind speed and sensor height for wind velocity spectra

5.2.6 *Types of Wind Noise*

In the following section, we discuss four types of wind-related "noise." More detailed discussions of this can be found in Shields (2005), Raspet et al. (2006), and Raspet et al. (2006).

5.2.6.1 Wind Velocity Fluctuations

For the inertial subrange, Monin and Yaglom (1975) show that the power density spectrum of the wind velocity in the downwind direction is

$$V_{11}(k_1) = a_2 \varepsilon^{2/3} k_1^{-5/3}, \tag{5.5}$$

where a_2 is a constant and k_1 is the wave number in the wind direction assuming Taylor's hypothesis

$$k_1 = 2\pi f / \overline{u} \tag{5.6}$$

Recent observations have shown that the −5/3 power laws accurately describes the velocity spectra in the inertial subrange (Shields 2005; Raspet et al. 2006).

5.2.6.2 Interactions Between the Sensor and the Wind

As an object deflects wind, kinetic energy is converted into pressure energy. The pressure at the head of the body directly in front of the wind is called the "stagnation pressure" and is the maximum pressure on the body due to the deflection of the wind. Fluctuating wind velocity can therefore give rise to fluctuating stagnation pressure on pressure-sensing surfaces. Raspet et al. (2006) derived two equations for the stagnation pressure density spectrum in the inertial subrange. Because stagnation pressure depends on the bluffness and geometry of the sensor, effects that are easier to determine empirically than theoretically, they suggest that recorded wind-velocity spectra can be used to predict stagnation pressure and the upper limit of recorded infrasound wind noise in the inertial subrange. Specifically, the stagnation pressure is

$$P_s(k_1) = \rho^2 \overline{u}^2 \left| \overline{V(k_1)} \right|, \tag{5.7}$$

where P_s is the stagnation pressure power density and $\left|\vec{V}\right|$ is the power spectral density of the recorded wind velocity magnitude. A second equation for the stagnation pressure is

$$P_s(k_1) = 1.14\rho^2 \left(\overline{u}^2 + 3.67\overline{u^2}\right) \left(\frac{V_{11}(k_1^0)}{(k_1^0)^{-5/3}} \right) k_1^{-5/3} - 5.89 \left(\frac{V_{11}(k_1^0)}{(k_1^0)^{-5/3}} \right) k_1^{-7/3}, \tag{5.8}$$

where the quantity $V_{11}(k_1^0)$ is the power spectral density of the wind velocity in the downwind direction evaluated for a reference wave number k_1^0 at which there is a good fit of a −5/3 power law curve to the spectra of recorded wind velocity in the downwind direction, and

$$\overline{u^2} = \frac{1}{3}\left(\overline{u_x^2} + \overline{u_y^2} + \overline{u_z^2}\right) \tag{5.9}$$

is the mean of the mean of the squared velocities in the downwind, crosswind, and vertical directions. Predicting P_s is potentially advantageous in the testing of wind-noise reduction methodologies since it eliminates the need for a reference pressure sensor. However, use of the aforementioned equations in the inertial subrange requires a research-grade anemometer that is capable of output sampling rates that are commonly used for microphones (at least 20 Hz). Many of the current IMS anemometers are not capable of such high output rates.

Equations (5.7) and (5.8) are only valid in the inertial subrange. Raspet et al. (2006) extended the turbulence–sensor interaction theory into the source range and introduced

$$P_s(k_1) = \frac{1.44\overline{u}^2 C}{\left[1+(k_1\lambda)^2\right]^{5/6}} + \frac{1.451C^2}{\lambda\left[1+0.1129(k_1\lambda)^2\right]^{5/6}}, \tag{5.10}$$

where C and λ are fit parameters, the latter of which being a length parameter that reflects the location of the transition from the source region to the inertial subrange. These two fit parameters are determined by fitting of the following function to the downwind velocity spectrum

$$V_{11}(k_1) = \frac{C}{\left[1+(k_1\lambda)^2\right]^{5/6}} \tag{5.11}$$

Note that the first term of the pressure equation is simply the velocity spectrum multiplied by $1.44\overline{u}^2$. The second term is constant for low wave numbers and decays as $k_1^{-5/3}$ for high wave numbers. The authors verified that in the inertial subrange, the predictions from equation (5.10) match those from equations (5.7) and (5.8).

5.2.6.3 Pressure Anomalies Advected Across the Sensor

Turbulence–Turbulence Interaction

Taylor's hypothesis predicts that pressure anomalies that develop in turbulent flow in the absence of sensor interference (that is characterized by turbulence–sensor interaction) may be advected with the mean wind speed across a sensor, leading to another type of wind noise. There have been two possible sources of these advected pressure anomalies discussed in the literature. George et al. (1984) describe these sources based on a review of published measurements and identifications of different

pressure fluctuations sources from a turbulent jet without interference from noise associated with wind/sensor interaction. Pressure anomalies can be generated due to the interaction between turbules. Miles et al. (2004) show that this "turbulence–turbulence interaction" is the dominant source of turbulence-induced pressure in the inertial subrange above some threshold sensor height.

Dimensional analysis has been used to derive the pressure power spectral density for turbulence–turbulence interaction, as shown in Monin and Yaglom (1975)

$$P_t(k_1) = a_1 \rho^2 \varepsilon^{4/3} k_1^{-7/3}, \tag{5.12}$$

where a_1 is a constant. This −7/3 pressure power law was also derived by analytical techniques (Hill and Wilczak 1995). However, Miles et al. (2004) found using "Large Eddy Simulation" that this law needs further evaluation for cases where the atmosphere is thermally stratified and stable (strongly positive z/L).

More recently, two equations have been derived that permit the prediction of the turbulence–turbulence pressure spectrum from the velocity spectrum in the inertial subrange. Batchelor (1951) and Raspet et al. (2006) derive

$$P_t(k_1) = 7.60 \left(\frac{V_{11}(k_1^0)}{(k_1^0)^{-5/3}} \right) k^{-7/3} \tag{5.13}$$

Miles et al. (2004) also calculated a velocity and pressure power density from a "large eddy simulation" (LES) and fit their synthetic data and statistics from their simulations to scaling laws based on work by Obukhov (1941). They derive

$$P_t(k_1) = 10.2 \left(\frac{V_{11}(k_1^0)}{(k_1^0)^{-5/3}} \right)^2 k^{-7/3} \tag{5.14}$$

The aforementioned equations are only valid in the inertial subrange, and as with equation (5.8), one must evaluate the velocity spectrum at a reference wave number k_1^0 where the −5/3 power law fits the velocity spectrum well. Raspet et al. (2008) extended the theory to the source region, resulting in

$$P_t(k_1) = 0.811 \frac{C^2}{\lambda} \frac{1}{\left[1 + 0.1792 (k_1 \lambda)^2\right]^{7/6}} \tag{5.15}$$

At low wave numbers, the predicted pressure spectrum is constant, whereas at high wave numbers, the spectrum decays as $k_1^{-7/3}$.

Turbulence–Mean Shear Interaction

The vertical gradient of the average horizontal wind velocity near the ground acts as an impedance to turbules. Turbulence in this region creates another source of pressure fluctuations called "turbulence–mean shear interaction." Raspet et al. (2006) also developed an empirical equation for this that is valid in the source region and inertial subrange,

$$P_{\mathrm{m}}(k_1) = 7.38CK^2 \frac{\lambda^2 (k_1\lambda)^{5/3}}{\left[1+1.622(k_1\lambda)^2\right]^{8/3}} \tag{5.16}$$

In contrast with the constant spectra at low wave numbers for turbulence–sensor and turbulence–turbulence interaction, the turbulence–mean shear interaction spectrum increases as $k_1^{5/3}$ to a peak just before the transition to the inertial subrange where it decays as $k_1^{-11/3}$.

Correlation Distance of Turbulence

Shields (2005) examined pressure and wind data from 28 piezoelectric microphones on the ground and spaced parallel and perpendicular to the dominant wind direction at three field sites. He expanded upon previous results (e.g., Priestley 1966) and derived a model for the narrow-frequency-band correlation of recorded pressure as a function of sensor separation in the downwind and crosswind directions for the 0.2–2.0 Hz range. These correlations are the cross-correlations at zero lag time; these equations have no bearing on Taylor's hypothesis and only describe the spatial structure of turbulence during a snapshot in time.

$$R(x) = \mathrm{e}^{-3.2x} \cos(2\pi x) \tag{5.17}$$

and

$$R(y) = \mathrm{e}^{-7y} \cos(2\pi y) \tag{5.18}$$

where x and y are the separations in unit wavelength, which is defined by the sensor separation divided by the advective wavelength

$$\lambda = \overline{u_x} / 2\pi f \tag{5.19}$$

This is just the inverse of the advective wave number k_1 (5.6). Figure 5.7 shows Shields' results. The similarity between the measurements in each graph indicates that the spatial coherence length is linearly proportional to the size of the turbules over a wide range of length scales. In other words, the spatial characteristics of turbulence have a self-similar appearance. For example, defining the coherence length by the minimum distance to zero correlation, in 3 m/s wind, wind noise at 1 Hz has a coherence length of 0.1 and 0.3 m in the downwind and crosswind directions, respectively. In the same wind, the coherence lengths at 0.1 Hz are 1 and 3 m. Similarly, doubling the wind speed doubles these coherence lengths.

Of fundamental importance, Shields' results confirm the lower and slightly frequency-dependent results of Priestley (1966) that there is an exponential decay in the correlation in all directions (including vertical), but that the downwind direction has an additional periodic factor that oscillates about the zero axis. These results predict that spatial averaging of infrasound along a line parallel to the wind direction, rather than along any other line, results in the greatest attenuation of wind

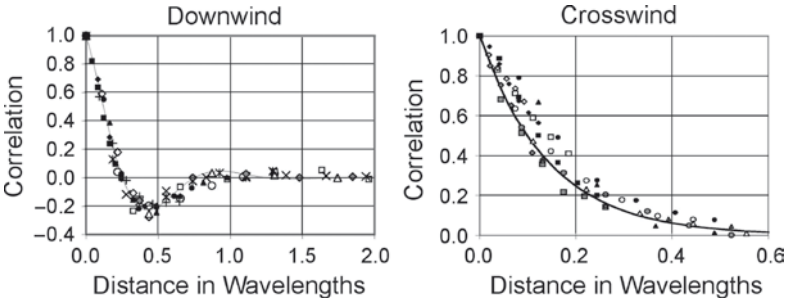

Fig. 5.7 Measured pressure correlation coefficients as a function of unit wavelength in the downwind and crosswind directions for three different field sites and central frequencies from 0.2 to 2.0 Hz. There is a periodicity to the correlation in the downwind direction. The graphed curves are the fits to lower-frequency data in Priestley (1966). Modified from Shields (2005)

noise associated with turbulence–sensor, turbulence–turbulence, and turbulence–mean shear interaction. Specifically, for frequencies where the sensor separation is greater than the coherence length as defined above, one will get approximately $n^{1/2}$ reduction in wind noise for the crosswind direction, but better than $n^{1/2}$ for the downwind direction providing that the sensor separation is not so large as to exclude the negative lobe in the correlation function. Shields specifically reports a "better than $n^{1/2}$" for the 0.5–5.0 Hz range in the downwind direction for his sensor spacing in the 4–8 m/s wind speed range (wind speed was recorded at 3 m height).

5.2.6.4 Acoustic Energy Generated by Wind

It is well known that the interaction of wind with objects can lead to acoustic energy radiation. At larger scales, it has been shown that wind can interact with mountain peaks to radiate infrasound in the 0.01–0.1 Hz band that can travel great continental distances (Larson et al. 1971; Rockway et al. 1974). Turbulent storm systems can also radiate infrasound (e.g., Gossard 1956; Bowman and Bedard 1971; Georges and Greene 1975).

Wind can also indirectly generate infrasound. For example, as the winds increase, so do the size of ocean swells, which can lead to higher surf and more energetic surf infrasound (Garcés et al. 2003; Arrowsmith and Hedlin 2005) and the interaction of intersecting swell patterns (microbaroms; e.g., Garcés et al. 2004). Furthermore, wind also leads to seismic disturbances, which can couple into infrasound via seismic-to-acoustic coupling or create artificial pressure signals if the infrasound sensor is sensitive to seismic shaking.

5.2.6.5 Distinguishing between Wind Noise Types

In designing and testing wind-noise reduction technologies, it is helpful to understand the type of wind noise one is recording and attempting to reduce. Using the

aforementioned equations may help as they predict distinctly different spectra with unique slopes. For example, the recent Raspet et al. (2006) predictions for turbulence–sensor (TS), turbulence–turbulence (TT), and turbulence–mean shear (TMS) interaction suggest that at a height of 1 m, in order of increasing influence in the contribution to wind noise is TMS, TT, and TS for the inertial subrange. In the source range, the contribution to wind noise is TT, TS, and TMS. More observations are required to tests these relations at different heights and at lower frequencies, but Raspet et al. (2006) found that 0.6 and 1.0 m spherical microphone wind screens attenuated wind noise to the same level as that predicted by turbulence–turbulence interaction in the inertial subrange, suggesting that successively larger wind screens would not provide additional improvement.

Similarly, Raspet et al. (2006) analyzed some data presented by Shields (2005). Figure 5.8 shows the pressure spectra recorded by a variety of sensors with different exterior shapes and sizes: (a) a bare B&K 1/2-inch microphone, (b) a piezoelectric sensor, (c) a microphone in a 0.18 m windscreen, and (d) a microphone in a 0.90 m windscreen. Predicted spectra are plotted for turbulence–sensor interaction (a and b), turbulence–turbulence interaction (c and d), and self-noise for the 0.18 and 0.90 m windscreens (E and F). The bare microphone has a spectrum that is fairly close in amplitude and slope to that predicted by the turbulence–sensor interaction. This predicted spectrum serves as an upper limit on the expected wind noise given no wind-noise reduction filters.

Wind noise predicted by turbulence–turbulence interaction correlates with that measured by the 0.9 m windshield sensor (d). However, this may be a coincidence

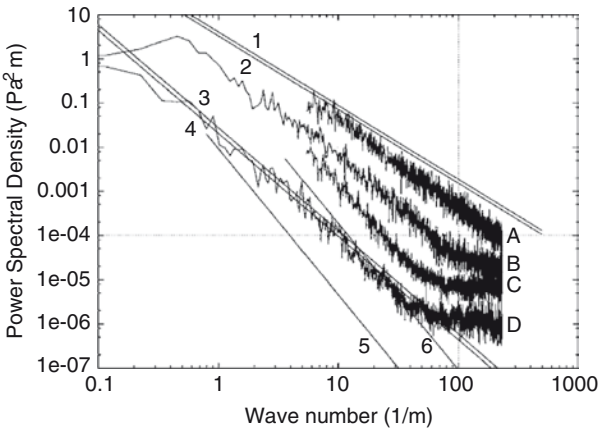

Fig. 5.8 Power spectral densities of wind-noise pressure recordings from four different sensors (A–D) compared with six predictions of wind-noise pressure spectra (1–6). Recordings are made with a bare B&K 1/2-inch microphone (**a**), a piezoelectric sensor (**b**), a microphone in a 0.18 m windscreen (**c**), and a microphone in a 0.90 m windscreen (**d**). Predictions are for Raspet et al. turbulence-sensor interaction (1–2), Batchelor turbulence-turbulence interaction (3), Miles et al. turbulence-turbulence interaction (4), self-noise for the 0.18 m windscreen (5), and self-noise for the 0.90 m windscreen (6). Slightly modified from Raspet et al. (2006)

given that the height of the anemometer was at 1 m while the pressure sensor in the 0.9 m ball was at 0.45 m, meaning that the wind noise predictions were for a higher elevation than those of the sensor.

The pressure spectra recorded by the piezoelectric sensors are about 20 dB greater than that predicted by turbulence–turbulence interaction. If the turbulence–turbulence predictions are accurate, this suggests that the dominant mechanism for the wind noise recorded by Shields is not due to the advection of pressure anomalies across the microphone. Shields collocated one of the piezoelectric sensors with a B&K microphone inserted in a Quad Disk enclosure. A Quad Disk is a tube with four disks mounted over four holes in such as way as to provide a point inside the tube where one can measure pressure that is independent of wind speed and direction (Nishiyama and Bedard 1991). Wyngaard et al. (1994) developed a technique to predict the effect of velocity variations on pressure measurements, and he showed that the Quad Disk should be insensitive to turbulence–sensor interaction. Shields argues that the spectra obtained by both the B&K and the piezoelectric sensors were similar, suggesting that the piezoelectric sensor was not measuring turbulence–sensor noise. Shields also reports that the magnitude of pressure in the 0.5–2.5 Hz band recorded by the piezoelectric sensors at all three sites falls within an upper and lower bounds estimated by Bedard et al. (1992) by analyzing three months of Quad Disk pressure data recorded in various winds. These data show a scatter of up to 10 dB between the bounds, which is considerably less than the 20 dB difference between Shields observations and the turbulence–turbulence prediction, suggesting that the piezoelectric sensors are not greatly influenced by wind–sensor interaction. Based on the good fit of the turbulence–turbulence predictions with the wind-screened microphones, Raspet et al. interprets the piezoelectric sensors to be quite aerodynamic and dominated by fluctuations of a smaller stagnation pressure.

5.3 Wind-Noise Reduction Methodologies

Wind-noise reduction technologies seek to reduce all types of wind noise while preserving signal energy. Most of the strategies to date have focused on reducing turbulence–sensor, turbulence–turbulence, and turbulence–mean shear interaction. As discussed earlier, these types of noise depend on the length scales of the turbules. As predicted by Taylor's hypothesis, the frequency of the noise from a single turbule with largest diameter d scales with the mean wind speed (e.g., Alcoverro and Le Pichon 2005).

The coherence of turbules varies as a function of size and distance traveled. An acoustic signal propagates at much faster velocities and may remain coherent at separations of kilometers. Most of the wind-noise reduction strategies are based on the contrasting spatial coherence lengths of turbules and acoustic signals. The technologies can be grouped into four classes: acoustic integration filters, instantaneous integration sensors, digital filtering with dense microphone arrays, and wind/sensor isolation strategies.

5.3.1 Daniels Filter

There have been a number of mechanical filters developed that attach to microbarometers or low-frequency microphones. If atmospheric pressure is sampled at a number of locations (n) spaced far enough apart so that the pressure variations from wind noise are uncorrelated, but close enough such that the acoustic signal remains coherent and in phase, summing the time series will increase the noise power by n and the signal power by n^2, resulting in a power signal-to-noise improvement of n (or $n^{1/2}$ in amplitude). This is the basis for the seminal work Fred Daniels performed in the 1940s and 50s, leading to the Daniels wind filter, which is also the basis of two other filter designs described later (Daniels 1952, 1959).

The Daniels filter comprises a series of different tapered pipes with sensing inlets distributed uniformly along its length and a microphone connected to its wide end (Fig. 5.9). It is designed to detect coherent infrasound as it propagates from left to right along the length of the filter. Provided that $rf^{1/2}$ is large, where r is the pipe radius and f is the signal frequency, the wave speed inside the pipe will match the wave speed outside, and the signals inside the pipe will sum in phase provided the narrow end of the pipe is pointing directly toward the source. These diameters also acoustically scale the coherent infrasound signals that propagate toward the central microphone such that the acoustic summation of the coherent signals at the microphone yields the outside signal pressure amplitude. While the filter sums signal in phase, incoherent noise from the inlets that travels acoustically inside the pipe is attenuated due to the scaling. The individual pipes have carefully selected diameters and inlet impedances to inhibit internal resonance. A prototype filter was ~600 m long with 100 equally spaced openings. The pipe inner diameter ranged from ~40 mm near the microbarometer to ~8 mm. The noise reduction was reported to be on the order of 20 dB in times of high winds (up to 12 m/s).

The Daniels filter is effectively a line microphone. It has an omnidirectional infrasound instrument response for wavelengths larger than four times the length of the filter ($f < 0.14$ Hz in the 600-m long prototype). For shorter wavelengths, the response is anisotropic and a function of the angle between the signal direction and the pipe (Olson 1947; Daniels 1959; Cook and Bedard 1971; Noel and Whitaker 1991). Figure 5.10 demonstrates the instrument response for three angles. For a broadband signal entering the filter and propagating toward the sensor at the same speed (Fig. 5.10a), the signal is recorded perfectly (flat instrument response). For the opposite direction (Fig. 5.10b), the signals that entered the inlets do not arrive at the sensor in phase, and the response is a boxcar function in time, which is a sinc function in frequency. For the broadside direction (Fig. 5.10c), the signals are also

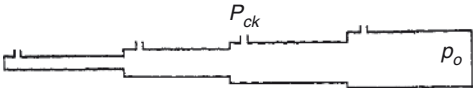

Fig. 5.9 The Daniels wind filter. A microbarometer connects to the wide end of the pipe. From Daniels 1959

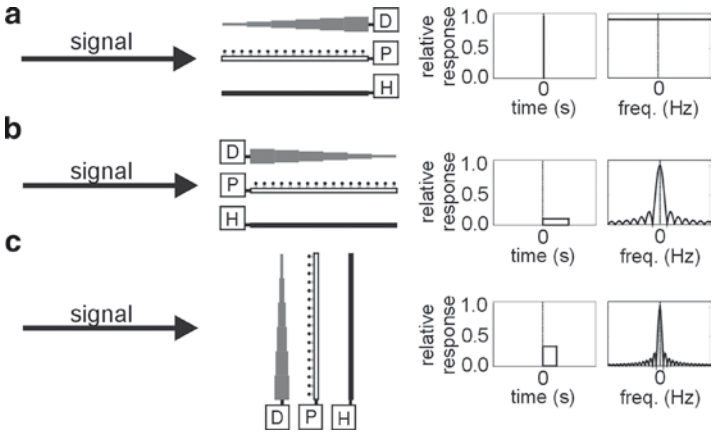

Fig. 5.10 Simplistic view of a Daniels (D), pipe (P), and porous hose (H) filter response to an infrasound signal due to acoustic integration of the signal that enters the filter at various points along its length. For the case of the filter pointing toward the source (**a**), the signal is recorded perfectly leading to a delta function and flat impulse response in the time and frequency domains, respectively. For the opposite case (**b**), one gets the most attenuation of the signal, leading to a wide boxcar and sinc function. For broadside ensonification (**c**), the boxcar is half the width in time of (**b**). In reality, the response for the microporous hose is more complex

out of phase at the sensor, but not by as much, leading to a narrower boxcar function and a broader sinc function. Other more isotropic pipe configurations have been considered (e.g., circular pipes studied by Burridge 1971 and Grover 1971).

5.3.2 Rosette Pipe Filters

A rosette filter is an extension of the Daniels filter and comprises an areal array of solid pipes that are interconnected to a central microbarometer to provide an omnidirectional infrasound instrument response and wind-noise reduction in a frequency band that depends on the aperture of the filter.

The rosette filter is the standard wind-noise filter used at IMS array sites and was designed by Alcoverro in the late 1990s (Alcoverro 1998; Alcoverro and Le Pichon 2005). The original design comprises a number of low-impedance inlets connected by solid pipes to a microbarometer where sound from all inlets is acoustically summed. The along-pipe distance from each inlet to the microbarometer is equal, and thus, at any moment, pressure at the microbarometer is the sum of pressure changes that entered each inlet of the filter simultaneously. The sum is unweighted as each inlet has the same low impedance, which is scaled based on the number of inlets in the filter. In other words, the filter response is a delta function of unity amplitude for vertically incident infrasound.

The inlets are arranged in a geometrically regular pattern around a circle and spaced far enough apart to provide nearly omnidirectional $n^{½}$ noise reduction for a particular frequency band. Alcoverro's prototype filter is shown in Fig. 5.11 and comprises 32 inlets spanning an area 16 m across. The maximum *SNR* gain with this filter is 15 dB. The band of noise reduction possible with each filter scales with aperture. Larger filters provide greater separation of sensors to provide the requirement of incoherent wind noise at lower infrasound frequencies. More recent designs used at IMS sites range in diameter from 18 to 70 m, with considerably more inlets (up to 144). In the filter pictured in Fig. 5.11, noise reduction of 15 dB is observed from 0.1 to 10 Hz. In tests at the Piñon Flat Observatory, Hedlin et al. (2003) found that at wind speeds up to 5.5 m/s, the 18 m filter reduced noise by as much as 20 dB above 0.2 Hz; a 70 m filter reduced noise by a similar amount between 0.02 and 0.7 Hz.

Resonance is an issue inherent in rosette filters. The rosette filter connects each inlet to the microbarometer via two pipes. These pipes are joined at the "secondary summing manifold" (Fig. 5.11). The acoustic impedance of the path is thus not

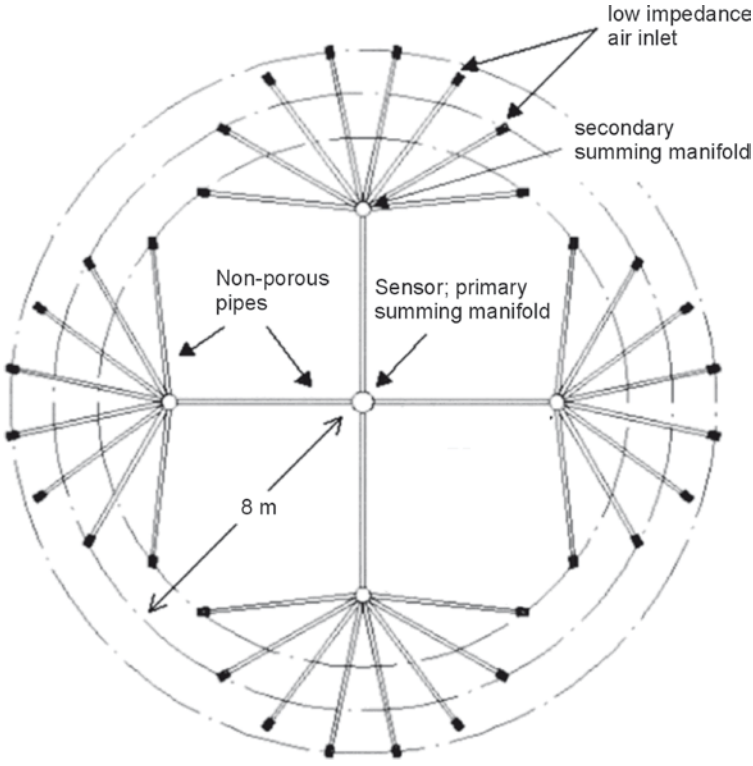

Fig. 5.11 Prototype rosette noise-reduction filter. The salient feature of this filter is that signals and noise are summed at a microbarometer located at the center of the filter after an identical propagation time delay from the inlets for vertically incident signals. Modified from Alcoverro and Le Pichon (2005)

constant giving rise to resonance of different frequencies in each pipe. The fundamental frequency of the resonance scales with the pipe length and is nearly independent of wind speed and temperature. For the 70-m filter, the lowest fundamental frequency is 2.65 Hz, well within the band of interest. Resonance in the shorter pipe is predicted to lie above 9 Hz. Resonance is observed at all wind speeds (Hedlin et al. 2003).

As predicted by Alcoverro and Le Pichon (2005) and demonstrated by Hedlin and Alcoverro (2005) the lower-frequency resonance can be eliminated by installing impedance matching capillary plugs in each pipe that leads away from the microbarometer adjacent to the secondary summing manifolds (Fig. 5.12). These capillary units are solid cylinders of a certain length of PVC that are drilled along their axes to create holes (capillaries) of a certain diameter. The length and diameter of these capillaries are calculated precisely to match the dimensions of the pipe such that they inhibit reflections back to the microbarometer. These small capillaries must be clear of obstructions however, since blockage would close off a significant part of the array from the primary summing manifold. It is unknown how partial or total blockage of one or more capillaries would affect the rosette response. The resonance in the shorter pipes can also be eliminated in a similar fashion, but such a retrofit is costly and usually not necessary if the band of interest is only for frequencies below 5 Hz.

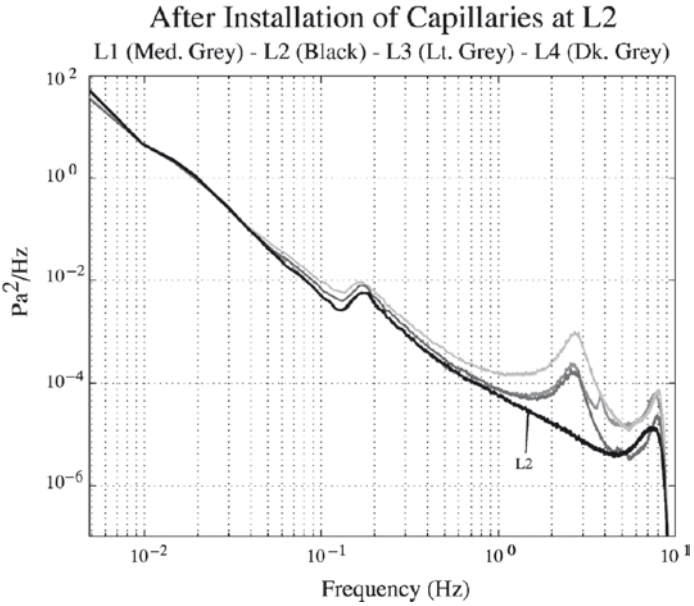

Fig. 5.12 Spectral density estimates taken from data collected without impedance matching capillary plugs (*grey curves*) and with capillary plugs installed at all secondary manifolds (curve labeled "L2"). The microbarom peak can be seen in all spectra at 0.2 Hz. The capillaries effectively remove the resonance in the main pipes between the primary and secondary manifolds. From Hedlin and Alcoverro (2005)

We now return to the omnidirectional instrument response of a rosette. Although the response is a delta function with unity amplitude for vertically incident signals, typical infrasound signals propagate across the filter at grazing elevation angles (<15°; McKisic 1997) and are heavily attenuated because the signals that enter each inlet do not arrive to the central microbarometer in phase. This can be modeled by calculating the travel time it takes for a plane wave that propagates across all the inlets to travel through the pipes to the central sensor. For each of the 32 travel times (for the filter in Fig. 5.11), a delta function of 1/32 amplitude is created and added to the time domain response at the correct time with respect to the time the wavefront crosses the central sensor. The resulting magnitude of the Fourier transform of the response is shown in Fig. 5.13. Smaller 18-m rosettes do not attenuate infrasound below 10 Hz but reduce wind noise by as much as 20 dB above 0.2 Hz. Larger 70-m rosettes do not attenuate infrasound below 2 Hz, but reduce wind noise by up to 20 dB between 0.02 and 0.7 Hz. These "high-frequency" and "low-frequency" rosettes have the fundamental limitation that they can only provide about 20 dB of wind-noise reduction because they cannot be made larger without pushing the flat part of the infrasound signal response to lower frequencies.

An array of small and large rosettes provides the means to monitor the 0.02–10 Hz infrasound band with roughly up to 20 dB wind-noise reduction. Standard array-processing techniques like beamforming can be used to provide an additional *SNR* gain. However, such techniques only work well with array elements that use the same type of rosette filter or in the low-frequency signal band common to all rosettes.

A potential issue with rosette filters is that the pipe diameter can be too small. As the pipe diameter decreases, the pipe should become more dispersive to internally propagating infrasound (Benade 1968). It is our understanding that this effect has not been empirically measured or quantified; the filter responses shown in Fig. 5.13 are approximations (that do not include dispersion) of the actual filter response.

Rosettes are expensive to fabricate and deploy. Depending on the material with which they are constructed and the array location, maintenance costs can also be expensive. Most of the IMS network pipes are either made of PVC or galvanized metal, which usually gets brittle or attacked by corrosion over time. Some of the newly installed IMS rosettes are made of stainless steel pipe and non-corrosive inlets. Because the pipes are open to the atmosphere, occlusions can develop in the capillaries or pipes, the detection and location of which is time consuming. Finally, rosettes occupy a considerable amount of space, which is an especially important consideration for island stations where space is at a premium.

5.3.3 Microporous Hoses

Much infrasound data in recent years has been collected via 1.6-cm diameter microporous or "soaker" hoses that are designed for irrigation. Depending on the objective, configurations vary from linear porous hoses to circular ones, all con-

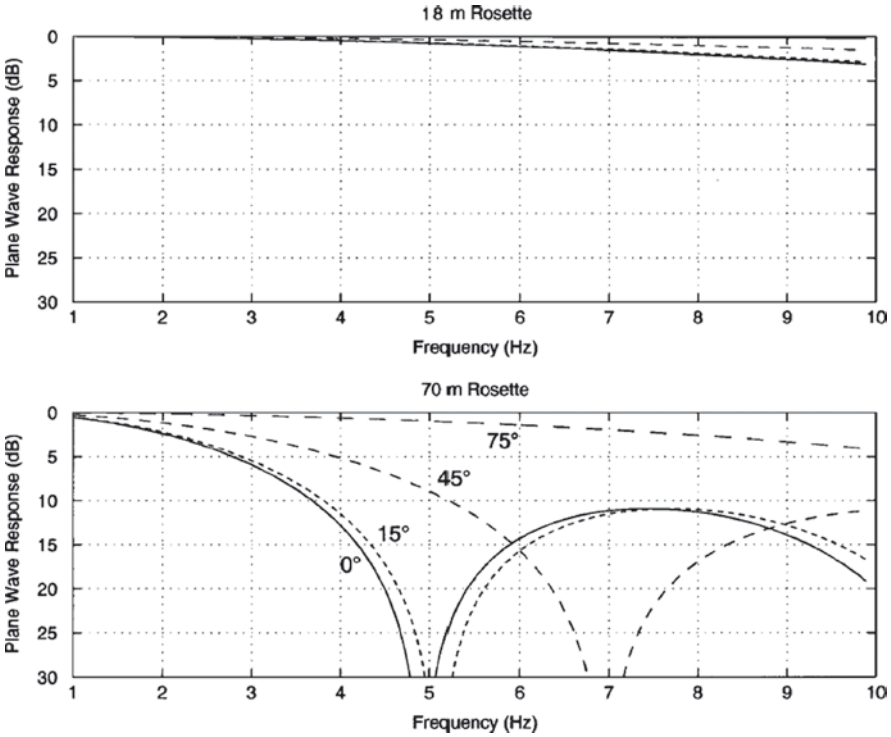

Fig. 5.13 The upper and lower panels show the plane-wave response for the 18- and 70-m rosette filters, respectively, at four arrival angles. The solid curves in each panel represent the response to horizontally propagating signals. The finely to coarsely dashed curves represent signals propagating across the two filters at 15°, 45°, and 75° above the horizontal. The elevation angles are calculated assuming a sound speed of 347 m/s. From Hedlin et al. (2003)

nected to a central or end microbarometer (e.g., Fig. 5.14). There is presumably destructive interference in incoherent wind noise for turbules that are smaller than either the length of the hose for linear configurations or the aperture for areal configurations.

For linear configurations, the instrument response of a porous hose is presumed to be qualitatively similar to that of a Daniels or single pipe filter (Fig. 5.10); as the signal wavefront propagates along the length of the hose toward the microphone, a running acoustic wave presumably propagates inside the hose at the same speed. Ideally, the signal is recorded perfectly, leading to an instrument response characterized by a delta function. The amplitude of this delta function is important. If the signal is originating from the summation of signals that diffused into all parts of the hose, then the hose should have a signal gain factor that increases with hose length. If there is no significant signal gain effect, this suggests that the hose may be analogous to a windscreen commonly found on microphones, which reduces wind noise but may not lead to greater wind-noise reduction with longer hoses.

Fig. 5.14 Photo of a spiraling-outward microporous hose connected to a microbarometer at Piñon Flat Observatory

A circular, spiral, or several linear porous hoses radiating from a central microphone are often used for applications where the source direction is unknown a priori. Such a configuration makes the filter's instrument response and wind-noise reduction isotropic for all signal azimuths and wind directions, which simplifies array processing.

This filter has fared well under some empirical tests. In a study of underground nuclear tests at the Nevada Test Site, Noel and Whitaker (1991) considered various configurations of porous hoses (e.g., "spiders" comprising several microporous arms radiating from the microbarometer, and crosses, a type of spider filter with just four orthogonal arms). They concluded that the spider and cross designs effectively reduced noise while causing relatively little distortion of the signals in the frequency band of interest. Haak and de Wilde (1996) also found significant noise reduction in the band from 10 s to 10 Hz.

These filters are commonly used at temporary recording sites where the goal is to record for a relatively short period of time (e.g., days to weeks/months) for a relatively low cost. The filters are inexpensive, both in terms of raw material cost and manpower. However, using these filters is now being discouraged for long-term installations, and even some short-term ones, for several reasons. First, the theoretical instrument response of a porous hose is not well understood and has not been successfully modeled. Howard et al. (2007) presented results that suggested above ~20 Hz, low-frequency acoustic signals do not penetrate the hose well. They also found that signals coming from the broadside do not have such a simple sinc function response as shown in Fig. 5.10c and are attenuated across the band. Signals propagating along the length were found to be amplified in the 10–20 Hz range

(Fig. 5.10a). They also made measurements at 1, 5, and 10 Hz in an anechoic chamber that suggest infrasound input into the end of the filter is attenuated as it propagates inside at a rate that increases with increasing frequency (up to 1.1 dB/m at 10 Hz). Surprisingly, removing the cap at the end of 18 m long hoses did not appear to significantly affect the response (Hetzer, personal communication, 2008). Finally, they clearly showed that different hoses of the same length and width had significantly different responses and roll-off frequencies, presumably due to different ages or manufacturers. This leads one to wonder if the instrument response is also time dependent, changing with increasing exposure to ultraviolet radiation, dust, and rain.

Porous hoses are also fragile. A single pin-sized hole close to the end where the microphone is can generate high noise levels (Herrin, personal communication, 2006). A kink, which is easy to create and often hard to mend, is also likely to create resonance or other anisotropic instrument-response peculiarities.

5.3.4 Optical Fiber Infrasound Sensor

The previous summation filters relied on acoustic summation of signals that impact many inlets (pipes or flexible hoses) or pores (microporous hoses). The rosettes reduce wind noise, but as they get larger, the omnidirectional instrument response for typical infrasound signals is degraded. The optical fiber infrasound sensor (OFIS) directly measures the integrated pressure change along a path; this sensor does not rely on the propagation of pressure signals through a narrow tube to a central manifold. A laser shines through two optical fibers that are helically wrapped around a long, sealed 2.54 cm diameter silicone tube in such a way as to create a Mach-Zender interferometer that measures diameter change of the tubular diaphragm due to a passing pressure wave. The fiber-wrapped tube is encased in insulation and placed inside a perforated drainage tube of 10 cm diameter (Fig. 5.15). Calibration experiments have been performed demonstrating that the sensor has a flat instrument response down to a frequency dependent on the size of a vent hole (typically 0.05 Hz) and up to the kHz range for broadside signals. Unlike the rosettes, acoustic resonance inside the tube is not measured, since standing waves are averaged to zero by the instantaneous integration along the length. These sensors can lie on the surface, but their sensitivity is currently a function of temperature; they perform well when buried in a trench beneath at least 15 cm of gravel. Lab and field measurements indicate that below 20 Hz there is no attenuation of infrasound by the gravel (Zumberge et al. 2003). Several comparisons with collocated MB2000 sensor recordings show that they are relatively insensitive to seismic shaking likely because such shaking generally modifies the shape of the tube and not the volume that it occupies.

Zumberge et al. (2003) buried a 90-m long linear OFIS beneath 15 cm of gravel at Piñon Flat Observatory and collected several weeks worth of data with which to compare the OFIS to the collocated 70-m L2 pipe rosette of the I57US array.

Fig. 5.15 Photo of the optical fiber infrasound sensor. The sensor is a 2.54 cm diameter silicone tube wrapped with two optical fibers. A laser shines through the fibers. The sensor measures pressure induced diameter changes of the silicone tube with laser interferometry

A microporous hose was laid out around the periphery of the L2 rosette. The I57US L2 and porous hose filters were connected to MB2000 microbarometers. A rocket launch occurred at nearby Vandenberg Air Force Base. The three sensors yielded nearly identical recordings. Figure 5.16 shows the power spectral density computed from a 15 min time window for two mean wind speeds. In 1.4 m/s winds, the OFIS noise floor is about the same as the other systems below 1 Hz. Above 1 Hz, the OFIS is about 10–20 dB lower than that of L2 and the porous hose. In moderate winds (3.4 m/s), the OFIS has a noise floor that is the same as that provided by the porous hose, both of which are lower than L2, likely due to the resonance. Plotting the minimum power for each frequency after computing 440 power spectra shows the same relationships.

The results presented in Zumberge et al. (2003) compare the OFIS to the L2 array element. In moderate winds, the OFIS and porous hose are comparable. As mentioned earlier, the response of the porous hose is unknown, so it is unclear how useful the entire hose was for this comparison. Resonance makes comparison with L2 difficult. Recent comparisons with L2, after it was fitted with capillaries to remove the 3 Hz resonance peak, suggest that in moderate wind a 90-m linear OFIS reduces wind noise at roughly the same level as the 70-m L2 rosette (Walker et al. 2007a, b).

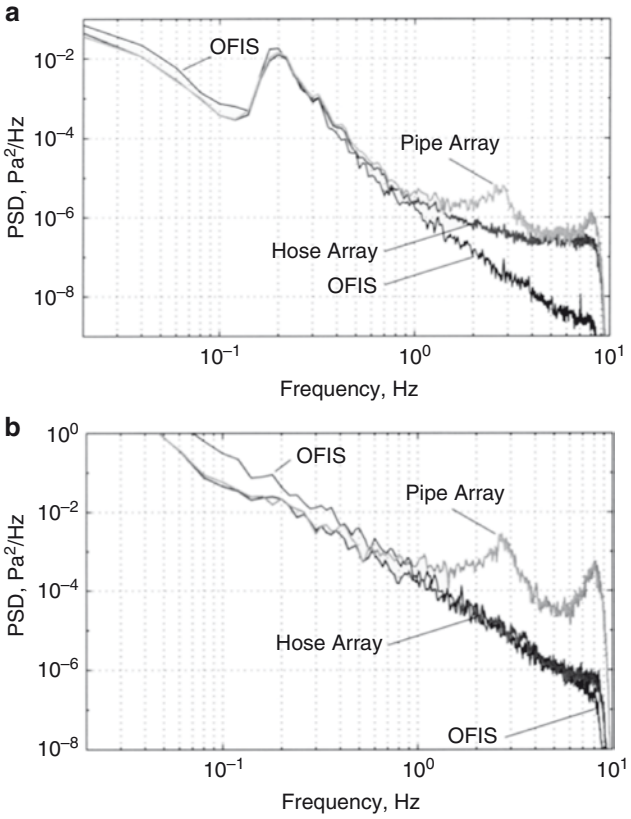

Fig. 5.16 Comparison of the OFIS sensor to the low-frequency element of the I57US array. The power spectral densities are shown for a single 15-min time window for a mean wind speed of 1.4 m/s (**a**) and 3.4 m/s (**b**). The resonance peaks in the L2 rosette are apparent at about 3 and 8 Hz. Modified from Walker et al. (2008)

Recent tests have shown that the minimum noise of L2 is due to the self-noise of the microbarometer. Therefore, once L2 is fitted with a better microbarometer or microphone it should perform better than that shown in Fig. 5.16a in low wind conditions. The self-noise of an OFIS depends on its length, but is generally on the order of $10^{-10}\,\mathrm{Pa^2/Hz}$ for frequencies above 0.2 Hz. For frequencies below 0.2 Hz, the noise floor goes up to $5\times10^{-7}\,\mathrm{Pa^2/Hz}$ at 0.05 Hz presumably due to thermal noise. The noise floor was determined by measuring the noise in the interferometer by helically wrapping the fiber on a stiff mandrill that is not sensitive to atmospheric pressure change. Therefore, the OFIS noise floor in Fig. 5.16b likely represents the acoustic noise floor for that time period at I57US.

An OFIS is similar to the other acoustic summation filters in that it is a directional sensor if used in a linear configuration. Figure 5.17 shows the instrument response of an OFIS as compared to that of a 90-m pipe array. For infrasound with wavelengths larger than $4L$, where L is the length of the linear OFIS, the OFIS is

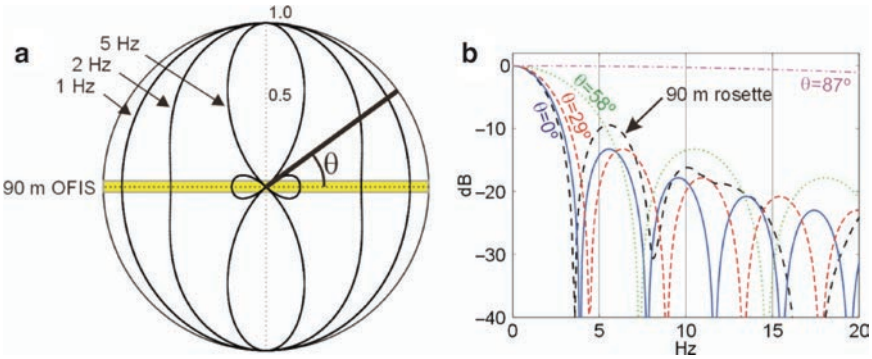

Fig. 5.17 Directivity (**a**) and frequency response (**b**) for a 90-m long OFIS as a function of and frequency. In (**a**) the response is plotted in polar coordinates as a function of θ for three example frequencies. In (**b**) the response is plotted in dB as a function of θ and frequency for four example angles. For comparison purposes, the omnidirectional plane-wave response for a 90-m diameter rosette with eight, 16-m diameter secondary rosettes is also shown for grazing angles in (**b**). Modified from Walker et al. (2008)

effectively a point sensor and has an omnidirectional response (Fig. 5.17a). For shorter wavelengths, the response is more anisotropic. For signals impacting the broadside of the OFIS, the instrument response is a delta function of unity amplitude (flat response in frequency). For signals propagating along the length of the OFIS (endfire), there is a directional attenuation that depends on the frequency and length of the OFIS. The response is the exact opposite to that of the Daniels filter (Fig. 5.10) and has similarities to that of a rosette filter of the same size (Fig. 5.17b). The first node in a 90-m OFIS instrument response for an endfire signal matches the first node in a 90-m diameter rosette for all directions with grazing elevation angles. As mentioned, however, for near broadside signals, the OFIS response is nearly flat. This is a fundamental difference between an OFIS and a rosette; a cluster of several OFIS arms in a radial configuration can each provide wind-noise reduction roughly just as well as a single rosette of the same diameter that occupies the same space, but depending on the number and length of OFIS arms, at least one of the arms can record a broadband signal (0.05–10 Hz) from all directions without attenuation. Therefore, it is probable that a cluster of radially oriented OFIS arms may be an improved alternative to a rosette, since one can make such an OFIS cluster much larger than a rosette to get better wind-noise reduction but without limiting the ability to make broadband infrasound recordings. An additional difference between a rosette and an OFIS is that not only is wind noise from advected turbules attenuated, but wind-induced acoustic noise is also attenuated by the arms that are not oriented favorably to this arriving energy (just like infrasound signals would be).

The new OFIS design uses polarization maintaining fiber, which rectifies an issue with previous OFIS designs where polarization change of the light in the two fibers led to an occasionally uptime problem. Methods and software have been developed to calculate back azimuth and phase velocity by exploiting sensor directivity with a

small array of OFIS arms (Walker et al. 2008). A six-OFIS array near San Diego, California, has been operating since April 2008 for research and monitoring interests. Finally, an automated calibration system has been developed for each OFIS arm.

Current OFIS research is focused on two fronts. The first is on the level of wind-noise reduction provided by a buried OFIS, especially as a function of OFIS length, burial depth, gravel diameter, and wind direction. The second is on determining why the sensitivity to pressure change of an OFIS is a predictable function of temperature and OFIS length. Lab measurements have shown that the mechanical properties of short (1.5 m) silicone tubes do not change significantly with temperature. Field tests have shown that the sensitivity is not related to a buildup of differential pressure across the tube walls. Although the burial of the OFIS with the automated calibration system eliminates this from being a major nuisance, additional experiments and mathematical models are being developed that will likely lead to the fabrication of an OFIS that is insensitive to temperature.

5.3.5 *Distributed Sensor (Adaptive Processing with a Dense Array)*

Another approach to reducing wind noise is to record pressure simultaneously at many points sampled by a dense array. One could either record to disk all the traces and extract a signal of interest in post-processing, or one could use on-the-fly algorithms to reduce wind noise through filtering or weighted-averaging schemes that adapt to the changing wind conditions, outputting a single trace. This system has been labeled the "distributed sensor" and is being developed by the University of Mississippi and Miltech Research and Technology. The array sensors (Fig. 5.18) comprise similar piezoelectric microphones that are described in Shields (2005). Two configurations are being tested: wired and wireless. The wireless configuration communicates pressure samples through a nearest-neighbor approach, bouncing from one sensor to another until the sample reaches the data-logging hub. If one sensor stops working, communication automatically gets routed around that sensor.

Dillion et al. (2007) deployed a rectangular distributed sensor of 100 elements at Piñon Flat Observatory inside the 70-m L2 I57US rosette, which comprised 144 inlets. They occupied an area of ~500 m^2 inside the ~2,700 m^2 area of the rosette. They confirmed that for simple unweighted-averaging schemes, one gets the expected reduction of wind-noise power by roughly 20 dB. They also confirmed that the larger area and/or number of inlets for L2 reduce wind noise by roughly 5 dB more for frequencies above 0.8 Hz and below 0.4 Hz.

The true potential of the distributed sensor will probably be realized as we learn more about the physics of wind noise. For example, Shields (2005) found that averaging microphones along the wind direction can yield better than $n^{½}$ reduction wind noise. A simple approach would be to have an array of some given size and average only those sensors along a single line that is parallel with the current wind direction. A more sophisticated approach might involve weighted-averaging schemes.

For example, a sensor in the array could be summed with another sensor in the downwind direction a distance of 0.4 wavelengths away by an amount determined by the graph in Fig. 5.7 such that the average cancels the advected wind noise while preserving any energy that propagates across the sensor at a much faster acoustic velocity. Another approach might be a running frequency-wave number (F-K) filter that selectively attenuates slower moving energy that propagates across the array from all directions simultaneously, after which the resulting filtered data could be simply averaged. These are all techniques that might be invoked on a high-speed digital signal processor at the site or back in the lab after the data have been stored to disk. As the availability of faster computational and data storage resources increases with time, it should become easier to manage and process larger amounts of infrasound data.

The distributed sensor is reported to be relatively inexpensive and portable. The individual sensors are very durable, do not have resonance issues in the infrasound band, and have flat instrument responses. Over the next several years, a considerable effort will be spent on investigating if array processing techniques on data from such an array can provide better signal-to-noise ratios than a single rosette or an array of several rosettes.

5.3.6 Porous Media Filters

The last class of filters that we discuss may embody a completely different approach to wind-noise reduction, depending on the type of the wind noise being filtered. Instead of averaging over a number of sensing surfaces, one may be able to isolate the sensor from the advected turbules. Since wind speed decreases with distance toward the ground and the stagnation pressure is not defined on a flat ground for a horizontal wind, it may be that burial of wind sensors in a porous media like sand or gravel may provide a useful wind filter. Herrin et al. (2001) presented theory on wind-noise reduction in rigid, porous media and tested the theory with an experiment in a box of sand. They state that results of Attenborough (1983), Attenborough et al. (1986), and Sabatier et al. (1986, 1993) imply that infrasound pressure decreases exponentially with depth inside a semi-infinite half-space. They also state that "wind-generated atmospheric pressure changes" (presumably those that are advected across the ground) decrease exponentially with depth in this porous medium. Because the attenuation operators are different, the change in signal-to-noise ratio with respect to the observation at the surface, changes with depth

$$\Delta SNR(d) = \mathrm{e}^{d(\alpha_\mathrm{w} - \alpha_\mathrm{i})},$$

where α_i and α_w are the infrasound and wind attenuation operators

$$\alpha_\mathrm{i} = \mathrm{Re}\left(\sqrt{i\frac{\gamma\sigma\omega}{\rho_\mathrm{o}c_\mathrm{o}^{\,2}}}\right)$$

and

$$\alpha_{\mathrm{w}} = \mathrm{Re}\left(\sqrt{k_{\mathrm{w}}^2 + i\frac{\sigma\omega}{P_{\mathrm{o}}}}\right),$$

where γ is the specific heat ratio for air, σ is the effective flow resistance of the porous solid, ω is angular frequency, ρ_{o} is the air density, c_{o} is the sound speed, k_{w} is the horizontal wave number characterizing the wind turbules, and P_{o} is the pressure. Herrin et al. (2001) show that the signal-to-noise ratio does not change with depth for frequencies well below

$$f_{\mathrm{c}} = \frac{\sigma c_{\mathrm{w}}^2}{2\pi P_{\mathrm{o}}},$$

where c_{w} is the advective wind speed. For much higher frequencies,

$$\Delta SNR(d,\omega) = 20Log(e)\frac{\omega d}{c_{\mathrm{w}}}$$

The SNR increases with increasing frequency and depth for porous media that have appropriate effective flow resistances.

Herrin et al. (2001) collected data to test the above theory by empirically measuring the attenuation operators. They attached a microphone to a flexible hose, which they placed inside a $2.4\times2.4\times0.6$ m box of sand resting on the surface with the inlet in the center buried beneath 0.36 m of sand. They placed a reference hose and inlet inside the box at a depth of 0.05 m beneath the sand, right above the deeper inlet. They acquired data in both low and moderate winds. They found that they could fit an exponential decay curve to the wind-noise pressure using 6 and 12 m/s wind speeds for the low and moderate wind speed bins into which they separated the data. Unfortunately, no infrasound signals were detected during this trial, and consequently neither the infrasound attenuation operator nor the effective flow resistance could be verified.

Herrin et al. (2001) performed a second experiment where the dimensions of the first were roughly doubled. The burial depth of the test inlet was 0.84 m and the reference inlet was at a depth of 0.1 m. The analysis of this data set was also limited. However, they determined that over the wind speeds sampled, the average attenuation of wind noise was 40 dB at 1 Hz. As with the last data set, broadband infrasound signals were not recorded. However, microbaroms (0.15–0.3 Hz) were recorded during calm periods and used to empirically estimate the theoretical flow resistance of the sand of ~2.0×10^5 N s/m^4. With that flow resistance parameter, an infrasound decay curve was calculated and compared with the mean wind-noise attenuation curve. Although the infrasound transmission decays considerably with increasing frequency, the wind-noise transmission decays much faster beginning at 0.1 Hz and extending to 4 Hz where both curves intersect. This suggests an *SNR* increase of ~20 dB at 1 Hz for their inlet buried at 0.84 m. This also suggests that

above 4 Hz, the infrasound is attenuated more than wind noise. It appears that more work needs to be done in this area, but that porous media filters have significant potential as wind-noise filters, especially when used with sensors that have very low self-noise.

5.3.7 Wind Barriers

Wind barriers share similarities with porous media filters, since they attempt to isolate the sensors from the wind. This should greatly reduce noise from turbulence–turbulence and turbulence–mean shear interaction. The interaction of the barrier walls with the wind may lead to turbulence-sensor noise (i.e., the walls act as pressure sensing surfaces) depending on the wall construction. If the turbulence–sensor noise is negligible and barriers do not create additional noise in the form of turbulence inside the enclosure, then they could be very effective, only measuring the acoustic noise generated by the wind.

There have been several wind barrier designs over the last two decades. Liszka conducted pioneering work with wind barriers for noise reduction at infrasonic frequencies (e.g., Liszka 2008). In Liszka's patented wind barrier design (Swedish Patent No. 7315138-3, October 30, 1975) a sensor is placed inside a semiporous hexagonal barrier. The sides of the fence are not solid to avoid increasing large-scale turbulence downstream of the barrier.

Another design tested by Hedlin and Raspet (2003) included sides that were 50% porous and 2 m high by 5.5 m apart at the base. The entire barrier was coated with a fine wire mesh. The sensor was located inside foam at the center of the fence. The fence reduced wind speed by 90%. Surprisingly, the 10× reduction in wind speed inside the fence did not result in a proportional 20 dB reduction in infrasonic wind noise. In most of the frequency band of interest, the rosettes performed much better in reducing wind noise. However, noise reduction by the barrier was observed to be over 10 dB at frequencies above 0.5 Hz at low wind speeds (<0.5 m/s) and at frequencies above 2 Hz (at wind speeds above 4.0 m/s).

The Hedlin and Raspet (2003) work has an implication for the type of wind noise being created or reduced by the barrier. The wind-noise reduction by the barrier scales much like the wind-noise reduction of the rosettes produced by spatial averaging. Figure 5.19 shows the wind-noise reduction ratio (wind filter spectra divided by spectra from a reference port) for 5.25 m/s wind speed and different filter types with characteristic sizes L (70, 18, and 2.0 m for the rosettes and barrier). As stated by Hedlin and Raspet "If the wind noise and wind-noise reduction are caused by local interactions of the turbulence and the wind-noise reduction device (turbulence–sensor interaction), the wind-noise reductions of similar devices should scale as the ratio of the turbulence scale to a characteristic linear dimension of the device (Strasberg 1988)." Therefore, instead of plotting reduction ratio vs. frequency, they are plotted vs. the scaled "frequency" fL/v, where v is the mean wind speed. Consequently, Fig. 5.19 displays the relative effectiveness of the wind filter in

reducing wind noise generated by turbules with a length scale normalized by the length scale of the assumed spatial averaging filter.

Hedlin and Raspet show that the shapes of the curves, except for that part associated with the 70-m rosette resonance peaks, are independent of wind speed and have roll-offs to the rosettes if the scaling length for the barrier is the barrier height (2.0 m) instead of the barrier diameter (5.5 m). This may suggest that pressure fluctuations are primarily averaged over the front of the barrier in the wind in a similar fashion to being averaged over the surface of the rosettes. However, the barrier displayed a small but significant wind-noise reduction (4 dB) even when the size of the turbulence is greater than the size of the barrier itself (from a scaled frequency of 0.05 to 0.5). This additional noise reduction might be due to a mechanism similar to that of the spherical foam windscreens (Fig. 5.19) in which reductions occur because the pressure measured at the center is the area average of the pressures generated at the surface of the sphere; the wind barrier may serve as a pressure averaging device over the surface of the barrier with negative and positive contributions even for turbulent structures with dimensions much larger than the windscreen. If this is the case, a roof or a more spherical barrier may provide better wind-noise reduction. Regardless, this result suggests that the fundamental issue faced by wind barriers is the reduction in the noise generated by the interaction of the barrier itself with the turbules.

Solid-walled barriers tested by Shams et al. (2005) employed a variety of materials. The guiding principle in this design was that the solid walls, with a low acoustic impedance, would divert atmospheric turbulence away from the sensor while allowing long-period infrasound to penetrate to the interior. One design was found to reduce noise at 0.7 Hz by 10 dB and by greater than 20 dB at 20 Hz. Despite the solid sides, noise from vortex shedding was found to lie above 20 Hz.

A series of barriers have recently been designed and tested by Doug Christie (e.g., Christie et al. 2007; Christie and Campus 2010). The material used is outdoor windscreen that is roughly 50% porous. As of this writing his best design, in terms of experimentally measuring wind-noise reduction at IS07 Warramunga, is shown in Fig. 5.20. The hexagonal barrier has a diameter of 14 m, vertical sides of 2 m height, a roof, internal radial baffles to dampen internal vortices, and serrated edges that extend both outward and downward from the outer upper edge. The serrated edges were a development that came out of work on wind fences designed for an infrasound tornado-warning system network (Bedard et al. 2004) and are designed to reduce the generation of local turbulence as air flows up and over the barrier. Most of the other components of the barrier were designed to minimize air flow within the barrier.

Christie's barrier designs have evolved, with that in Fig. 5.30 being version 5. He reports a dramatic improvement in wind-noise reduction during the transition from a version with an open structure to one with a roof made of the same porous screen. He recorded data with this design using Chaparral Physics microphones and plotted stacked spectra in Fig. 5.21. Comparison of a reference pipe array outside the enclosure (and presumably far enough away to be out of the enclosure's wake) with an identical pipe array and a single inlet microphone inside the enclosure shows a dramatic reduction in wind noise, especially at high frequencies. As was

observed by Hedlin and Raspet (2003), the frequency above which the barrier performs well scales with wind speed. At 1 Hz, the wind-noise reduction is between roughly 5–20 dB for winds up to 5.7 m/s. Remarkably, in most cases, the wind-noise reduction is about the same for the inside pipe array as well as for the inside single inlet microphone, suggesting that a single microphone may be all that is required inside these enclosures.

It is clear that a wind barrier is more effective at reducing some type of wind noise than a 6-inlet pipe array of the same size. However, the technology is still young and there are interesting and practical questions that remain. For example, an 18-m rosette often has as many as 96 inlets, providing a 20 dB reduction in incoherent noise. Since one obtains 5–20 dB reduction at 1 Hz in wind up to 5.7 m/s simply with the enclosure, will that reduction add to that provided by an outside rosette of 96 elements, if that rosette was instead enclosed? In other words, would a rosette of 96 elements outside an 18-m enclosure reduce wind noise to the same base level as that which is provided by the enclosure over an identical 96-element rosette? If so, then there is no benefit to enclosing rosettes. In addressing these questions, spectra predictions from the aforementioned equations for the different types of noise could be invaluable and save lots of time in terms of field experimentation.

The signal-to-noise ratio is ultimately what one seeks to improve. Wind-noise reduction is therefore only half of the problem. The response of the enclosure to infrasound signals should probably be quantified. Christie et al. (2007) compared the time series of an infrasound signal that was recorded in windless conditions by a single port outside the enclosure and the pipe array and single port inside the

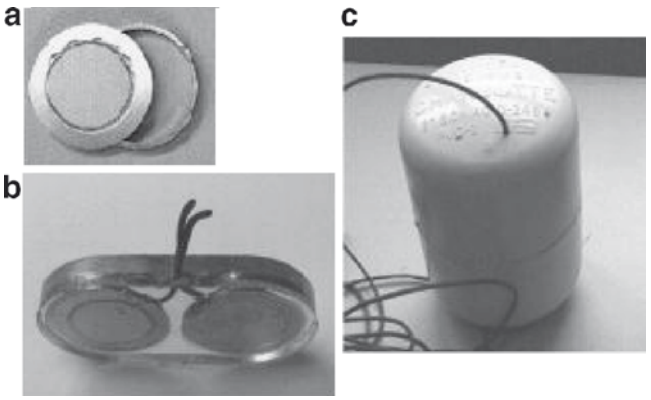

Fig. 5.18 Piezo-electric microphones used in the distributed sensor. (**a**) Pictures a piezoelectric "bimorph" formed by cementing a piezo-ceramic disc to a 3.5 cm diameter brass disc. A pressure sensitive capsule is formed by cementing one of these bimorphs to each side of the brass ring also shown. (**b**) Pictures two capsules, one with the piezo-ceramic turned out and one with it turned in, potted in transparent polyurethane. (**c**) Pictures the housing for the potted capsules. It is made from 5-cm diameter schedule 40 PVC pipe with end caps. The potted capsules are wrapped in fiberglass and enclosed in this PVC housing. Fifty-four holes are bored in the PVC housing in such a way as to make the sensor insensitive to seismic disturbances. From Shields (2005)

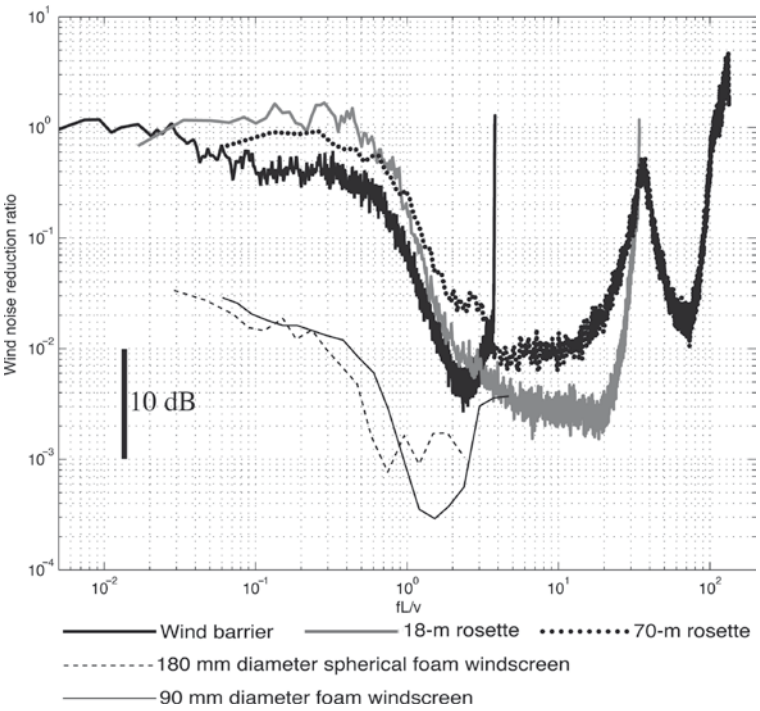

Fig. 5.19 Wind-noise reduction ratio (filter results divided by results from a reference port) vs. scaled frequency at 5.25 m/s for a 70-meter rosette (*bold dots*), for a 18-meter rosette (*bold grey*) and for a wind barrier (*bold black*). Also displayed is the noise reduction produced by a 90-mm-diameter foam windscreen at an average wind speed of 4.84 m/s (*light dashed curve*) and a 180-mm diameter spherical foam windscreen at 4.74 m/s (*light solid curve*). In this figure f is the time frequency, L is the scale length, and v is the wind speed. From Hedlin and Raspet (2003)

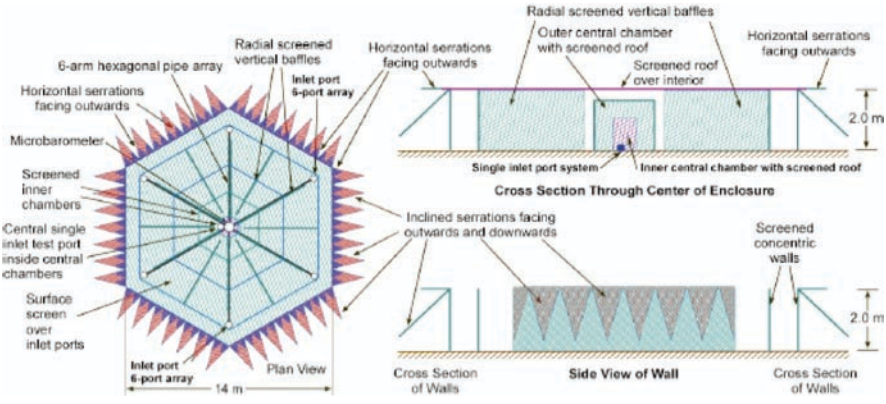

Fig. 5.20 Christie's wind barrier design (version 5). This 14-m barrier encloses a 6-inlet pipe array and a central reference microphone. Modified from Christie et al. (2007)

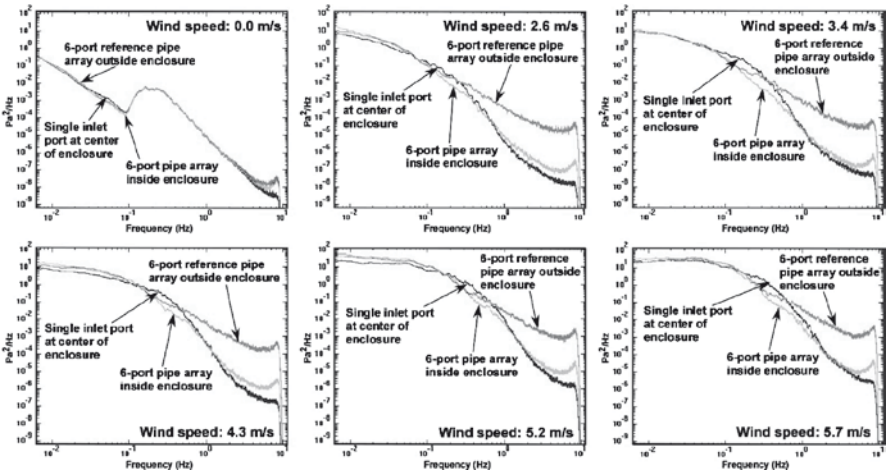

Fig. 5.21 Stacked noise spectra at wind speeds ranging from 0.0 to 5.7 m/s. Spectra are shown for three sensors: a single microphone inside the enclosure, a pipe array inside the enclosure, and the same size pipe array outside the enclosure. The sensors used are Chaparral Physics model 5 microphones with electronic noise floors that are not observed in any of these spectra. Modified from Christie et al. (2007)

enclosure. They showed that there is no attenuation for the dominant frequency of that signal, which was ~1 Hz (Christie et al. 2007). However, subtle differences observed in the structure of the recorded signals may suggest that higher frequencies were attenuated by the enclosure. As with rosette filters, knowledge of the enclosure response function is useful for determining how different properties of the enclosure may impact the ability to hear infrasound throughout the band of interest. For example, would reducing the permeability of the fabric or increasing the size of the enclosure by 20% lead to better wind-noise reduction at 1 Hz without attenuating infrasound at lower frequencies?

A few other questions remain. Can wind barriers (up to 14 m across) be tuned to perform as well as larger 70-m rosettes in the 0.05–0.7 Hz band? What level of improvement can be expected for large 70 m rosettes that have enclosures around the individual subrosettes? Finally, knowing what type of wind noise that is being reduced by these filters, perhaps with the help of the equations above, will help determine how well they will perform at other sites where the predominant wind noise type may be different.

5.4 Discussion

Some characteristics of the ideal infrasound station are that it occupies little space, has a low surface profile, has superb wind-noise reduction at all frequencies while faithfully recording signals, has the ability to determine accurately the direction of

arrival, is maintenance free, and is user-friendly to the station operator and data processor. The many methods discussed earlier exist because there are various situations where some of these characteristics are more important than others. However, many of these techniques are fairly young, not completely understood, and not yet proven to be mission capable.

Two of the technologies above have received considerable attention during the last decade: rosette and porous hose filters. It is probably fair to say that rosettes are currently the standard to which every other technology should be compared. However, it must be remembered that rosettes are inherently flawed by their omnidirectional attenuation of infrasound signals for grazing elevation angles. While this flaw does not affect small pipe arrays, it is debilitating for large arrays that have the ability for better wind-noise reduction, especially at lower frequencies. Porous hoses, although inexpensive and very portable, have been found to be unpredictable at best. Sometimes they provide wind-noise reduction comparable to a rosette. Sometimes they create their own noise. They too suffer from the omnidirectional attenuation of infrasound signals as the rosettes.

The other "younger" technologies may be well poised in the next several years to eventually replace or be used to retrofit aging rosettes and porous hoses arrays. For example, small existing rosettes should probably be retrofitted with wind barriers if such barriers can provide additional wind-noise reduction without signal degradation. This wind noise filter seems to be the most mature of the "young" technologies previously discussed, although outstanding questions still exist. The practical lifetime and maintenance requirements for such barriers are also undetermined.

Rosette footprints could be replaced with buried clusters of n OFIS arms or distributed sensors. The full potential of the distributed sensor may only become clear after different algorithms have been tested on trial data sets. As discussed above, a single OFIS of length L appears to reduce wind noise by about the same amount as a rosette of diameter L. A buried OFIS cluster that occupies the same horizontal area as a rosette should provide greater wind-noise reduction than the rosette if the OFIS time series are summed together or if only the OFIS oriented in the direction parallel to the wind is considered. Since each OFIS arm is a directional sensor that has a flat response for near broadside infrasound signals, one could also make an OFIS cluster much larger than a rosette to get even greater wind-noise reduction without compromising the ability of the sensor to make broadband infrasound recordings of signals from all directions. In this latter case, determining the direction of arrival with several of these OFIS clusters is accomplished with a conceptually simple modification to standard array processing algorithms. For example, the "trial direction" in beamforming would determine which OFIS in each cluster to use for the correlation function, which imparts no additional computation. For even greater directional resolution for signals with good signal-to-noise ratios, one could also take advantage of all OFIS arms by using instrument-response-dependent beamforming (Walker et al. 2008).

Two guiding principles for the design of infrasound stations on islands is to minimize wind noise and the station footprint. A single distributed sensor, OFIS cluster, compact wind barrier array, an array of microphones encased in porous media, or some hybrid of these may work best for these sites.

Site location can of course greatly affect the level of wind noise. Perhaps the optimum natural filter that exists is a dense forest. Forests have a high surface roughness length, greatly reducing wind and likely breaking up large-scale turbules into smaller turbules that can be attenuated better by spatial filters. Although mountains have been associated with low frequency infrasound noise in the 0.01–0.1 Hz range and may cause blockage of higher frequency infrasound, valleys or craggily surfaces may also be locations of relatively slow winds. Given that even stable winds can interact with objects to create infrasound or turbules that can saturate an array, it is important to locate array elements far from obstacles in the path of the wind. Finally, it is clear that wind noise is a site-specific problem. A noise survey at sites of interest for future permanent infrasound stations could be useful in the design of wind filters specifically tailored for those sites.

There are several pitfalls that can arise in wind-noise reduction research that can cause great delays in progress. First, the self-noise floors of the sensors must be significantly lower than that which is possibly achievable with the wind filter. For example, the MB2000 and MB2005 microbarometers have a nominal self-noise floor on the order of 10^{-7} Pa^2/Hz. This sensor noise is apparent at frequencies above ~1 Hz, which happens often when connected to porous hoses or pipe arrays in low wind conditions.

Another problem that can arise is occlusion of the narrow impedance matching capillaries or pipes in reference rosettes. The capillaries are often very narrow, which allows them to become easily occluded. The biggest problem that they present is that such occlusions may remain unnoticed for a long time while quietly degrading the rosette performance and wind-noise reduction comparisons. Perhaps periodically blowing a jet of air through each pipe at the primary summing manifold would be an effective maintenance strategy. A more informative technique may be to impart an instantaneous pressure differential into each pipe and measure the decay rate, which should be predictable and identical for all pipes.

Another potential issue is the development of technologies under the assumption that there is only one type of wind noise. Some types of wind noise may be more important than others depending on the filtering mechanism or atmospheric conditions. Similarly, the same wind speed does not necessarily yield the same level of wind noise. Winds associated with stable atmospheres (non-convecting) are predicted to give rise to significantly lower wind noise levels than winds associated with vigorous diurnal convection. Along the same lines, winds from one direction may give rise to a different level of noise than winds from another direction based on local and regional influences. For this reason, it is probably wise to search for variations in wind-noise spectra for a given wind speed before averaging such spectra. Furthermore, comparing wind-noise reduction spectra obtained at different sites without knowledge of the type of wind noise being attenuated may be deceiving. Although more work remains to be done in quantitatively predicting wind noise, simple equations that predict different types of wind noise are contained in this chapter and explained in more detail in Raspet et al. (2006, 2008). Comparing spectra plotted as a function of advective wave number $2\pi f/\bar{u}$ (or scaled frequency $fL/\bar{u}$) or investigating wind noise with a distributed sensor can be used to determine if the wind noise is acoustic or being advected across the filter (e.g., Hedlin and Raspet 2003).

Testing wind-noise reduction filters is two-sided; such filters are designed to attenuate wind noise more than infrasound such that the signal-to-noise ratio improves. The development of wind-noise filters benefits from quantitative analyses of the effect of the filter on infrasound signals from all directions. This should especially be important if a significant effort is spent on carefully calibrating sensors in the lab that ultimately will be used with these filters. One technique for estimating the infrasound filter response is to calculate the coherence function or transfer function on a time window that contains a broadband infrasound signal recorded by the test sensor/filter and two reference sensors without filters. The three sensors must be spaced far enough apart such that infrasound remains spatially coherent while wind noise is spatially incoherent. Coherence functions are calculated for all three pairs of time series. The near-unity amplitudes of the coherence function between the two reference sensors indicate the spectral bandwidth of the infrasound signal, which provides guidance for how to interpret the other two coherence functions between the test sensor and reference sensors. Used in this way, one can piece together the infrasound filter response by analyzing several signals that together span the frequency band of interest.

It seems clear that continued, paced research and independent validation of results is important to flush out the details of each technology and prove if the technologies are mission capable before great efforts are taken to implement these technologies as part of a routine operational setup. Such efforts would especially benefit from the establishment of one or more "standard" testing facilities, perhaps in different environments, where the nature and character of the wind noise can be quantified and routinely verified with precision instruments such as a high-sample-rate anemometer and a permanent dense microphone array. Such a facility would also benefit from an onsite, active-source infrasound calibration tool such as that provided by a rotary subwoofer (Garcés and Park 2007) or a large weatherproof subwoofer array (Walker et al. 2007b).

5.5 Conclusions

Progress in infrasound science and monitoring efforts suffers from high noise levels created by the wind. There are a number of mature technologies that are routinely employed to reduce wind noise. However, these technologies are of limited usefulness; noise levels in moderate winds are still deafening and instrument responses are not always ideal for typical infrasound signals. The impact to existing monitoring efforts is that at any one time, it is possible that a subset of the IMS network stations will be beset by high noise.

A number of new techniques to reduce wind noise have developed during the last several years. These development efforts were guided by two principles: the need to improve signal-to-noise ratio and the need for compact, low-maintenance designs. In the order in which they are presented earlier, these include the optical fiber infrasound sensor, the distributed sensor, rigid porous media filters, and wind

barriers. The optical fiber sensor is a line sensor, usually buried in gravel, that instantaneously averages pressure along its length. Each arm of a cluster of OFIS arms in a radial configuration has about the same wind-noise reduction as a rosette of the same aperture, but at least one arm can record infrasound from any direction without attenuation. An OFIS cluster can therefore be made larger to provide a better signal-to-noise ratio than what could ever be provided by a rosette. The distributed sensor is a low-profile, generally portable system that comprises many (at least 100) robust, broadband microphones in both a wired and wireless configuration. Methods are being developed and tested to digitally filter wind noise while preserving infrasound. Such algorithms might be run in post-processing or onsite with high-speed digital signal processors. Theoretical work has been carried out and partially tested that predicts rigid porous media like sand and gravel can be utilized with other sensors to improve the signal-to-noise ratio in a part of the frequency band of interest. Finally, wind barriers may act as massive microphone windscreens or as devices that isolate the sensor from advected wind noise. A 14 m prototype has been developed that provides much greater wind-noise reduction above 0.7 Hz than that provided by a 6-port pipe array of the same aperture. These technologies are still young, but may mature during the next five to ten years if paced research and independent validation of results continues, especially if one or more "standard" testing facilities can be agreed upon and developed.

There have been some recent developments in wind-noise theory. It is clear that there are at least four types of wind noise that are important in the infrasound band: turbulence–sensor interaction noise, turbulence–turbulence interaction noise, turbulence–mean shear interaction noise, and acoustic noise generated by the wind. The first three types of noise effectively advect with turbules across the sensor at the mean wind speed. That type of wind noise can be verified if wind-noise spectra plotted as a function of advective wave number collapses onto a single curve. The pressure spectra due to each type of wind noise can also be predicted by wind velocity spectra using simple equations. Wind-noise theory is still evolving and requires more research and validation. However, that which has been discovered should be useful in further development of wind-noise reduction technologies.

Acknowledgements We thank Rich Raspet and Doug Shields for clarifying discussions and an anonymous reviewer for constructive comments that improved this manuscript. This work was supported by the U.S. Army Space and Missile Defense Command.

References

Alcoverro B (1998) Acoustic filters design and experimental results. Proceedings Workshop on Infrasound. DASE, Commissariat à l'Energie, Bruyères-le-Châtel, France, 21–24 July 1998

Alcoverro B, Le Pichon A (2005) Design and optimization of a noise reduction system for infrasonic measurements using elements with low acoustic impedance. J Acoust Soc Am 117: 1717–1727

Arrowsmith SJ, Hedlin MAH (2005) Observations of infrasound from surf in southern California. Geophys Res Lett 32:L09810. doi:10.1029/2005GL022761

Attenborough K (1983) Acoustical characteristics of rigid fibrous absorbents and granular materials. J Acoust Soc Am 73:783–799

Attenborough K, Sabatier JM, Bass HE, Bolen LN (1986) The acoustic transfer function at the surface of a layered poroeleastic soil. J Acoust Soc Am 79:1353–1359

Batchelor GK (1951) Pressure fluctuations in isotropic turbulence. Proc Cambridge Philos Soc 47:359–374

Bedard Jr. AJ, Whitaker RW, Greene GE, Mutschlecner P, Nishiyama RT, and Davidson M (1992) Measurements of pressure fluctuations near the surface of the Earth. 10th Symposium on turbulence and diffusion, Portland, OR, September 29 – October, 1992, American Meteorological Society, 45 Beacon St, Boston, MA, pp. 293–296

Bedard Jr. AJ, Bartram BW, Entwistle B, Golden J, Hodanish S, Jones RM, Nishiyama RT, Keane AN, Mooney L, Nicholls M, Szoke EJ, Thaler E, and Welsh DC (2004) Overview of the ISNET data set and conclusions and recommendations from a March 2004 workshop to review ISNET data. U.S. National Oceanic and Atmospheric Administration, Environmental Technology Laboratory, Boulder, CO, p. 20

Benade AH (1968) On the propagation of sound waves in a cylindrical conduit. J Acoust Soc Am 44:616–623

Berman S, Stearns CR (1977) Near-Earth turbulence and coherence measurements at Aberdeen Proving Ground, Maryland. Boundary-Layer Meteorol 11:485–506

Bowman HS, Bedard AJ (1971) Observations of infrasound and subsonic disturbances related to severe weather. Geophys J Roy Astron Soc 26:215–242

Burridge R (1971) The acoustics of pipe arrays. Geophys J R astr Soc 26:53–69

Chen WF (1997) Handbook of structural engineering. CRC Press, Boca Raton, pp 12–50

Cook RK, Bedard AJ (1971) On the measurement of infrasound. Geophys J R Astr Soc 26:5–11

Christie D (1999) The infrasound segment of the CTBTO's international monitoring system. IUGG, XXII General Assembly, B.7 (abstract)

Christie DR, Campus P (2010) The IMS infrasound network: design and establishment of infrasound stations. This volume, pp. 27–72

Campus P, Christie DR (2010) Worldwide observations of infrasonic waves. This volume, pp. 181–230

Christie D, Kennett BLN, and Tarlowski C (2007) Advances in infrasound technology with application to nuclear explosion monitoring. Proceeding of the 29th monitoring research review. Los Alamos National Laboratory, Los Alamos, New Mexico, pp. 825–835

Daniels FB (1952) Acoustical energy generated by the ocean waves. J Acoust Soc Am 24:83

Daniels FB (1959) Noise-reducing line microphone for frequencies below 1 c/s. J Acoust Soc Am 31:529–531

deWolf DA (1983) A random motion model of fluctuations in a nearly transparent medium. Radio Sci 18:138–142

Dillion K, Howard W, Shields FD (2007) Advances in distributed arrays for detection of infrasonic events [abstract]. J Acoust Soc Am 122:2960

Evers LG, Haak HW (2010) The characteristics of infrasound, its propagation and some early history. This volume, pp. 3–26

Favre AJ, Gaviglio J, Dumas R (1962) Corrélations spatio-temporelles en écoulements turbulents. Mécanique de la turbulence (Coll Intern Du CNRS à Marseille), Paris, ed. CNRS, 419–445

Frenkiel FN, Klebanoff PS (1966) Space-time correlations in turbulence. In: Pai SI (ed) Dynamics of fluids and plasmas. Academic Press, New York. pp. 257–274

Garcés M, Willis M, Hetzer C, Le Pichon A, Drob D (2004) On using ocean swells for continuous infrasonic measurements of winds and temperature in the lower, middle, and upper atmosphere. Geophys Res Lett 31:L19304. doi:10.1029/2004GL020696

Garcés M, Hetzer C, Merrifield M, Willis M, Aucan J (2003) Observations of surf infrasound in Hawaii. Geophys Res Lett 30(24):2264. doi:10.1029/2003GL018614

Garcés M, Park J (2007) A rotary subwoofer as an infrasonic source. Infrasound Technology Workshop. Tokyo, Japan. 13–16 November
George WK, Beuther PD, Arndt REA (1984) Pressure spectra in turbulent free shear flows. J Fluid Mech 148:155–191
Georges TM, Greene GE (1975) Infrasound from convective storms. Part IV. Is it useful for storm warnings? J Appl Meteor 14:1303–1316
Goedecke GH, Auvermann HJ (1997) Acoustic scattering by atmospheric turbules. J Acoust Soc Am 102:759–771
Gossard EE (1956) Gravity waves in the lower troposphere over southern California, Report 709. Naval Electronics Lab, San Diego, CA
Grover FH (1971) Experimental Noise Reducers for an Active Microbarograph Array. Geophys J Roy Astr Soc 26:41–52
Haak HW, de Wilde GJ (1996) Microbarograph systems for the infrasonic detection of nuclear explosions, KNMI publication, WR 96–06
Hedlin MAH, Raspet R (2003) Infrasonic wind noise reduction by barriers and spatial filters. J Acoust Soc Am 114:1379–1386
Hedlin MAH, Alcoverro B, D'Spain G (2003) Evaluation of rosette infrasonic noise-reducing spatial filters. J Acoust Soc Am 114:1807–1820
Hedlin MAH, Alcoverro B (2005) The use of impedance matching capillaries for reducing resonance in rosette infrasonic spatial filters. J Acoust Soc Am 117:1880–1888
Herrin E, Sorrells GG, Negraru P, Swanson JG, Golden P, Mulcahy C (2001) Comparative evaluation of selected infrasound noise reduction methods. Proceedings of the 23rd Seismic Research Review. Los Alamos National Laboratory, Los Alamos, New Mexico, pp. 131–139
Hill RJ, Wilczak JM (1995) Pressure structure functions and spectra for locally isotropic turbulence. J Fluid Mech 296:247–269
Howard W, Dillion K, Shields FD (2007) Acoustical properties of porous hose wind noise filters. J Acoust Soc Am 122:2985
Kaimal JC, Eversole RA, Lenschow DH, Stankov BB, Kahn PH, Businger JA (1982) Spectral characteristics of the convective boundary layer over uneven terrain. J Atmos Sci 39:1098–1114
Kolmogorov AN (1941) Local structure of turbulence in an incompressible fluid at very high Reynolds numbers. Dokl Akad Nauk SSSR 30:299–303
Koracin D, Berkowicz R (1988) Nocturnal boundary-layer height: observations by acoustic sounders and predictions in terms of surface-layer parameters. Boundary-Layer Meteorol 43:65–83
Landau LD and Lifshitz EM (1959) Fluid mechanics: course of theoretical physics, vol. 6. Addison-Wesley Series in advanced physics. London, Paris, Frankfurt: Pergamon Press, p. 536
Larson RJ, Craine LB, Thomas JE, Wilson CR (1971) Correlation of winds and geographic features with production of certain infrasonic signals in the atmosphere. Geophys J R astr Soc 26:201–214
Lettau H (1939) Atmosphärische Turbulenz. Akademische Verlagsgesellschaft, Leipzig
Liszka L (2008) Infrasound: a summary of 35 years of infrasound research. Institutet for rymdfysik, IRF Scientific report 291, ISBN 978-91-977255-0-7
McBride WE, Bass HE, Raspet R, Gilbert KE (1992) Scattering of sound by atmospheric turbulence: Predictions in a refractive shadow zone. J Acoust Soc Am 91:1336–1340
McKisic JM (1997) Infrasound and the infrasonic monitoring of atmospheric nuclear explosions: a literature review, final report submitted to the DOE and Phillips Lab, PL-TR-97-2123
McDonald JA, Douze EJ, Herrin E (1971) The structure of atmospheric turbulence and its application to the design of pipe arrays. Geophys J R astr Soc 26:99–109
McDonald JA, Herrin E (1974) Properties of pressure fluctuations in an atmospheric boundary layer. Boundary-Layer Meteorol 8:419–436
Miles NL, Wyngaard JC, Otte MJ (2004) Turbulent pressure statistics in the atmospheric boundary layer from large-eddy simulation. Boundary-Layer Meteorol 113:161–185
Monin AS, Yaglom AM (1975) Statistical fluid mechanics: mecahnics of turbulence, vol. 2. MIT Press, Cambridge, p. 874
Monin AS, Obukhov AM (1954) Basic laws of turbulent mixing in the ground layer of the atmosphere. Trans Geophys Inst Akad Nauk USSR 151:163–187

Nishiyama RT, Bedard AJ Jr (1991) A Quad-Disc static pressure probe for measurement in adverse atmospheres: with a comparative review of static pressure probe designs. Rev Sci Instrum 62:2193–2204
Noel SD, Whitaker RW (1991) Comparison of noise reduction systems. Los Alamos National Lab report LA-12003-MS
Obukhov AM (1941) Spectral energy distribution in a turbulent flow. Izv Akad Nauk SSSR Ser Georgr I Geofiz 5:453–466
Olson HF (1947) Elements of acoustical engineering, 2nd edn. D. Van Nostrand Company, Princeton, NJ
Panofsky HA (1962) Scale analysis of atmospheric turbulence at 2 meters. Q J R Meteorol Soc 88:57
Panofsky HA, Dutton JA (1984) Atmospheric turbulence: models and methods for engineering applications. John Wiley, New York, p 397
Panofsky HA, Mazzola C (1971) Variances and spectra of vertical velocity just above the surface layer. Boundary-Layer Meteorol 2:30–37
Pidwirny M, Budikova D (2006) Local and regional wind systems. In: Cutler J (ed) Encyclopedia of Earth, Cleveland (Washington, DC: Environmental Information Coalition, National Council for Science and the Environment)
Priestley JT (1966) Calculation of the effectiveness of infrasonic line microphones for reducing wind noise. National Bureau of Standards Report 9380
Raspet R, Webster J, Dillon K (2006) Framework for wind noise studies. J Acoustic Soc Am 199:834–843
Rockway JW, Hower GL, Craine LB, Thomas JE (1974) Applications of ray-tracing to observations of mountain-associated infrasonic waves. Geophys J R astr Soc 35:259–266
Sabatier JM, Bass HE, Bolen LN, Attenborough K, Sastry VVSS (1986) The interaction of airborne sound with the porous ground: the theoretical formulation. J Acoust Soc Am 79:1345–1352
Sabatier JM, Raspet R, Frederickson CK (1993) An improved procedure for the determination of ground parameters using level difference measurements. J Acoust Soc Am 94:396–399
Shams QA, Zuckerwar AJ, Sealey BS (2005) Compact nonporous windscreen for infrasonic measurements. J Acoust Soc Am 118:1335–1340
Shields FD (2005) Low-frequency wind noise correlation in microphone arrays. J Acoust Soc Am 117:3489–3496
Strasberg M (1988) Dimensional analysis of windscreen noise. J. Acoust Soc Am 83:544–548
Taylor GI (1938) The spectrum of turbulence. Proc Roy Soc A164:476–490
Thuillier RH, Lappe UO (1964) Wind and temperature profile characteristics from observations on a 1400 ft tower. J Appl Meteorol 3:299–306
Walker KT, Zumberge MA, Hedlin MAH, Shearer P (2008) Methods for determining infrasound phase velocity direction with an array of line sensors. J Acoust Soc Am 124:2090–2099
Walker KT, Zumberge M, Hedlin M, Berger J, Shearer P (2007) Resolving infrasound signals with arrays of optical fiber infrasound sensors (OFIS): low wind noise, superb back azimuth (and elevation angle) resolution, and a compact design. Infrasound technology workshop. Tokyo, Japan. 13–16 November
Walker KT, Dzieciuch M, Zumberge M, and DeWolf S (2007) M-sequences and an array of speakers form a sensor calibrator down to 8 Hz: Application to the OFIS at the new Camp Elliott OFIS array. Infrasound technology workshop. Tokyo, Japan. 13–16 November
Wyngaard JC, Siegel A, Wilczak J (1994) On the response of a turbulent-pressure probe and the measurement of pressure transport. Boundary-Layer Meteorol 69:379–396
Zumberge MA, Berger J, Hedlin MAH et al (2003) An optical fiber infrasound sensor: A new lower limit on atmospheric pressure noise between 1 and 10 Hz. J Acoust Soc Am 113:2474–2479